Velocity filtered density function for large eddy simulation of turbulent flows

L. Y. M. Gicquel and P. Givi[a)]
Department of Mechanical and Aerospace Engineering, University at Buffalo, State University of New York, Buffalo, New York 14260-4400

F. A. Jaberi
Department of Mechanical Engineering, Michigan State University, East Lansing, Michigan 48824-1226

S. B. Pope
Sibley School of Mechanical and Aerospace Engineering, Cornell University, Ithaca, New York 14853-1301

A methodology termed the "velocity filtered density function" (VFDF) is developed and implemented for large eddy simulation (LES) of turbulent flows. In this methodology, the effects of the unresolved subgrid scales (SGS) are taken into account by considering the joint probability density function of all of the components of the velocity vector. An exact transport equation is derived for the VFDF in which the effects of the SGS convection appear in closed form. The unclosed terms in this transport equation are modeled. A system of stochastic differential equations (SDEs) which yields statistically equivalent results to the modeled VFDF transport equation is constructed. These SDEs are solved numerically by a Lagrangian Monte Carlo procedure in which the Itô–Gikhman character of the SDEs is preserved. The consistency of the proposed SDEs and the convergence of the Monte Carlo solution are assessed by comparison with results obtained by an Eulerian LES procedure in which the corresponding transport equations for the first two SGS moments are solved. The VFDF results are compared with those obtained via several existing SGS closures. These results are also analyzed via *a priori* and *a posteriori* comparisons with results obtained by direct numerical simulation of an incompressible, three-dimensional, temporally developing mixing layer. © *2002 American Institute of Physics.* [DOI: 10.1063/1.1436496]

I. INTRODUCTION

The probability density function (PDF) approach has proven useful for large eddy simulation (LES) of turbulent reacting flows.[1–15] The formal means of conducting such LES is by consideration of the "filtered density function" (FDF) which is essentially the filtered fine-grained PDF of the transport quantities. In all previous contributions, the FDF of the "scalar" quantities is considered: Gao and O'Brien,[3] Colucci *et al.*,[6] Réveillon and Vervisch,[7] and Zhou and Pereira[12] developed a transport equation for the FDF in constant density turbulent reacting flows. Jaberi *et al.*[8] extended the methodology for LES of variable density flows by consideration of the "filtered mass density function" (FMDF), which is essentially the mass weighted FDF. The fundamental property of the PDF methods is exhibited by the closed form nature of the chemical source term appearing in the transport equation governing the FDF (FMDF). This property is very important as evidenced in several applications of FDF for LES of a variety of turbulent reacting flows.[6–10,12] However, since the FDF of only the scalar quantities are considered, all of the "hydrodynamic" effects are

modeled. In all previous LES/FDF simulations, these effects have been modeled via "non-FDF" methods.

The objective of the present work is to extend the FDF methodology to also include the subgrid scale (SGS) velocity vector. This is facilitated by consideration of the joint "velocity filtered density function" (VFDF). With the definition of the VFDF, the mathematical framework for its implementation in LES is established. A transport equation is developed for the VFDF in which the effects of SGS convection are shown to appear in closed form. The unclosed terms in this equation are modeled in a fashion similar to that in the Reynolds-averaged simulation (RAS) procedures. A Lagrangian Monte Carlo procedure is developed and implemented for numerical simulation of the modeled VFDF transport equation. The consistency of this procedure is assessed by comparing the first two moments of the VFDF with those obtained by the Eulerian finite difference solutions of the same moments transport equations. The results of the VFDF simulations are compared with those predicted by the Smagorinsky[16] closure, and the "dynamic" Smagorinsky model.[17–19] The VFDF results are also assessed via comparisons with direct numerical simulation (DNS) data of a three-dimensional (3D) temporally developing mixing layer in a context similar to that of Vreman *et al.*[20]

This work deals with LES of the velocity field in a constant density, nonreacting flow. Consideration of the joint

---

[a)]Author to whom correspondence should be addressed. Telephone: (716) 645-2593 (ext. 2320); Fax: (716) 645-3875. Electronic mail: givi@eng.buffalo.edu

velocity-scalar FDF (or FMDF) in variable density, chemically reacting flows will be the subject of future work. It is in this context that the approach has its principal advantage: Convective transport (of momentum and species) is in closed form.

II. FORMULATION

In the mathematical description of incompressible (unit density) turbulent flows, the primary transport variables are the velocity vector, $u_i(\mathbf{x},t)$ ($i=1,2,3$), and the pressure, $p(\mathbf{x},t)$, field. The equations which govern transport of these variables in space (x_i) and time (t) are

$$\frac{\partial u_i}{\partial x_i}=0, \quad \frac{\partial u_j}{\partial t}+\frac{\partial u_i u_j}{\partial x_i}=-\frac{\partial p}{\partial x_j}+\frac{\partial \sigma_{ij}}{\partial x_i}. \quad (1)$$

For a Newtonian fluid, the viscous stress tensor σ_{ij} is represented by

$$\sigma_{ij}=\nu\left(\frac{\partial u_i}{\partial x_j}+\frac{\partial u_j}{\partial x_i}\right), \quad (2)$$

where ν is the kinematic viscosity and is assumed constant.

Large eddy simulation involves the spatial filtering operation[21–23]

$$\langle f(\mathbf{x},t)\rangle_L=\int_{-\infty}^{+\infty}f(\mathbf{x}',t)\mathcal{G}(\mathbf{x}',\mathbf{x})d\mathbf{x}', \quad (3)$$

where $\mathcal{G}$ denotes the filter function, $\langle f(\mathbf{x},t)\rangle_L$ represents the filtered value of the transport variable $f(\mathbf{x},t)$, and $f'=f-\langle f\rangle_L$ denotes the fluctuations of f from the filtered value. We consider spatially and temporally invariant and localized filter functions, thus $\mathcal{G}(\mathbf{x}',\mathbf{x})\equiv G(\mathbf{x}'-\mathbf{x})$ with the properties,[21] $G(\mathbf{x})=G(-\mathbf{x})$, and $\int_{-\infty}^{\infty}G(\mathbf{x})d\mathbf{x}=1$. Moreover, we only consider "positive" filter functions[24] for which all the moments $\int_{-\infty}^{\infty}x^m G(x)dx$ exist for $m\geq 0$. The application of the filtering operation to the instantaneous transport equations yields

$$\frac{\partial\langle u_i\rangle_L}{\partial x_i}=0,$$

$$\frac{\partial\langle u_j\rangle_L}{\partial t}+\frac{\partial\langle u_i\rangle_L\langle u_j\rangle_L}{\partial x_i}=-\frac{\partial\langle p\rangle_L}{\partial x_j}+\frac{\partial\langle\sigma_{ij}\rangle_L}{\partial x_i} \quad (4)$$

$$-\frac{\partial\tau_L(u_i,u_j)}{\partial x_i},$$

where $\tau_L(u_i,u_j)=\langle u_i u_j\rangle_L-\langle u_i\rangle_L\langle u_j\rangle_L$ denotes the "generalized SGS stresses."[18] These stresses satisfy[18]

$$\frac{\partial}{\partial t}[\tau_L(u_i,u_j)]+\frac{\partial}{\partial x_k}[\langle u_k\rangle_L\tau_L(u_i,u_j)]$$

$$=-\frac{\partial T_{ijk}}{\partial x_k}-\Pi_{ij}+P_{ij}-\varepsilon_{ij}. \quad (5)$$

In this equation, $T_{ijk}=\tau_L(u_i,u_j,u_k)-\nu(\partial/\partial x_k)[\tau_L(u_i,u_j)]$ is the SGS turbulent transport tensor where $\tau_L(u_i,u_j,u_k)=\langle u_i u_j u_k\rangle_L-\langle u_i\rangle_L\tau_L(u_j,u_k)-\langle u_j\rangle_L\tau_L(u_i,u_k)-\langle u_k\rangle_L\tau_L(u_i,u_j)-\langle u_i\rangle_L\langle u_j\rangle_L\langle u_k\rangle_L$.[18] The other terms are the SGS pressure-velocity scrambling tensor, Π_{ij}

$=\tau_L(u_i,\partial p/\partial x_j)+\tau_L(u_j,\partial p/\partial x_i)$, the SGS production rate tensor, $P_{ij}=-\tau_L(u_i,u_k)\partial\langle u_j\rangle_L/\partial x_k-\tau_L(u_j,u_k)\partial\langle u_i\rangle_L/\partial x_k$, and the SGS dissipation rate tensor, $\varepsilon_{ij}=2\nu\,\tau_L(\partial u_i/\partial x_k,\partial u_j/\partial x_k)$.

III. VELOCITY FILTERED DENSITY FUNCTION (VFDF)

A. Definitions

The "velocity filtered density function" (VFDF), denoted by P_L, is formally defined as

$$P_L(\boldsymbol{v};\mathbf{x},t)\equiv\int_{-\infty}^{+\infty}\varrho[\boldsymbol{v},\boldsymbol{u}(\mathbf{x}',t)]G(\mathbf{x}'-\mathbf{x})d\mathbf{x}',$$

$$\varrho[\boldsymbol{v},\boldsymbol{u}(\mathbf{x},t)]=\delta[\boldsymbol{v}-\boldsymbol{u}(\mathbf{x},t)]\equiv\prod_{i=1}^{3}\delta[v_i-u_i(\mathbf{x},t)], \quad (6)$$

where δ denotes the delta function and $\boldsymbol{v}$ is the velocity state vector. The term $\varrho[\boldsymbol{v},\boldsymbol{u}(\mathbf{x},t)]$ is the "fine-grained" density,[11,25,26] and Eq. (6) defines the VFDF as the spatially filtered value of the fine-grained density. With the condition of a positive filter kernel,[24] P_L has all the properties of the PDF.[26] For further developments, it is useful to define the "conditional filtered value" of the variable $Q(\mathbf{x},t)$ by

$$\langle Q(\mathbf{x},t)|\boldsymbol{u}(\mathbf{x},t)=\boldsymbol{v}\rangle_L$$

$$\equiv\langle Q|\boldsymbol{v}\rangle_L=\frac{\int_{-\infty}^{+\infty}Q(\mathbf{x}',t)\varrho[\boldsymbol{v},\boldsymbol{u}(\mathbf{x}',t)]G(\mathbf{x}'-\mathbf{x})d\mathbf{x}'}{P_L(\boldsymbol{v};\mathbf{x},t)}, \quad (7)$$

where $\langle\alpha|\beta\rangle_L$ denotes the filtered value of α conditioned on β. Equation (7) implies

  (i)   for $Q(\mathbf{x},t)=c$, $\langle Q(\mathbf{x},t)|\boldsymbol{v}\rangle_L=c$,

  (ii)   for $Q(\mathbf{x},t)\equiv\hat{Q}(\boldsymbol{u}(\mathbf{x},t))$, $\langle Q(\mathbf{x},t)|\boldsymbol{v}\rangle_L=\hat{Q}(\boldsymbol{v})$,

  (iii)   Integral property:

$$\langle Q(\mathbf{x},t)\rangle_L=\int_{-\infty}^{+\infty}\langle Q(\mathbf{x},t)|\boldsymbol{v}\rangle_L P_L(\boldsymbol{v};\mathbf{x},t)d\boldsymbol{v}, \quad (8)$$

where c is a constant, and $Q(\mathbf{x},t)\equiv\hat{Q}(\boldsymbol{u}(\mathbf{x},t))$ denotes the case where the variable Q is completely described by the variable $\boldsymbol{u}(\mathbf{x},t)$. From these properties it follows that the filtered value of any function of the velocity variable is obtained by integration over the velocity space

$$\langle Q(\mathbf{x},t)\rangle_L=\int_{-\infty}^{+\infty}\hat{Q}(v)P_L(\boldsymbol{v};\mathbf{x},t)d\boldsymbol{v}. \quad (9)$$

B. VFDF transport equation

The exact transport equation for the VFDF is derived in this section. Two forms of this equation are considered similar to those previously developed in PDF methods.[27–31] The starting point is to consider the time-derivative of Eq. (6)

$$\frac{\partial P_L(\boldsymbol{v};\mathbf{x},t)}{\partial t} = -\int_{-\infty}^{\infty} \frac{\partial u_i(\mathbf{x}',t)}{\partial t}\frac{\partial \varrho[\boldsymbol{v},\mathbf{u}(\mathbf{x}',t)]}{\partial v_i}$$

$$\times G(\mathbf{x}'-\mathbf{x})d\mathbf{x}'. \tag{10}$$

This combined with Eq. (7) yields

$$\frac{\partial P_L(\boldsymbol{v};\mathbf{x},t)}{\partial t} = -\frac{\partial}{\partial v_i}\left[\left\langle \frac{\partial u_i}{\partial t}\middle|\boldsymbol{v}\right\rangle_L P_L(\boldsymbol{v};\mathbf{x},t)\right]. \tag{11}$$

Substituting Eq. (1) into Eq. (11) yields

$$\frac{\partial P_L(\boldsymbol{v};\mathbf{x},t)}{\partial t} = -\frac{\partial}{\partial v_i}\left\{\left[-\left\langle \frac{\partial u_i u_k}{\partial x_k}\middle|\boldsymbol{v}\right\rangle_L - \left\langle \frac{\partial p}{\partial x_i}\middle|\boldsymbol{v}\right\rangle_L\right.\right.$$

$$\left.\left.+\left\langle \frac{\partial \sigma_{ik}}{\partial x_k}\middle|\boldsymbol{v}\right\rangle_L\right]P_L(\boldsymbol{v};\mathbf{x},t)\right\}. \tag{12}$$

With the relation

$$\frac{\partial}{\partial v_i}\left[\left\langle \frac{\partial u_i u_k}{\partial x_k}\middle|\boldsymbol{v}\right\rangle_L P_L(\boldsymbol{v};\mathbf{x},t)\right] = -v_k\frac{\partial P_L(\boldsymbol{v};\mathbf{x},t)}{\partial x_k}, \tag{13}$$

and decompositions

$$v_k P_L = \langle u_k\rangle_L P_L + [v_k - \langle u_k\rangle_L]P_L,$$

$$\left\langle \frac{\partial p}{\partial x_i}\middle|\boldsymbol{v}\right\rangle_L P_L = \frac{\partial\langle p\rangle_L}{\partial x_i}P_L + \left[\left\langle \frac{\partial p}{\partial x_i}\middle|\boldsymbol{v}\right\rangle_L - \frac{\partial\langle p\rangle_L}{\partial x_i}\right]P_L,$$

$$\left\langle \frac{\partial \sigma_{ik}}{\partial x_k}\middle|\boldsymbol{v}\right\rangle_L P_L = \frac{\partial\langle \sigma_{ik}\rangle_L}{\partial x_k}P_L + \left[\left\langle \frac{\partial \sigma_{ik}}{\partial x_k}\middle|\boldsymbol{v}\right\rangle_L\right.$$

$$\left. -\frac{\partial\langle \sigma_{ik}\rangle_L}{\partial x_k}\right]P_L, \tag{14}$$

the VFDF transport equation becomes

$$\frac{DP_L}{Dt} = -\frac{\partial}{\partial x_k}\left[(v_k - \langle u_k\rangle_L)P_L\right] + \frac{\partial\langle p\rangle_L}{\partial x_i}\frac{\partial P_L}{\partial v_i}$$

$$-\frac{\partial\langle \sigma_{ik}\rangle_L}{\partial x_k}\frac{\partial P_L}{\partial v_i} + \frac{\partial}{\partial v_i}\left[\left(\left\langle \frac{\partial p}{\partial x_i}\middle|\boldsymbol{v}\right\rangle_L - \frac{\partial\langle p\rangle_L}{\partial x_i}\right)P_L\right]$$

$$-\frac{\partial}{\partial v_i}\left[\left(\left\langle \frac{\partial \sigma_{ik}}{\partial x_k}\middle|\boldsymbol{v}\right\rangle_L - \frac{\partial\langle \sigma_{ik}\rangle_L}{\partial x_k}\right)P_L\right], \tag{15}$$

where $D/Dt = \partial/\partial t + \langle u_k\rangle_L(\partial/\partial x_k)$ denotes the "filtered" material derivative.

Equation (15) is an exact transport equation for the VFDF. The first term on the right hand side represents the SGS convection of the VFDF in physical space and is closed. The second and third terms (which are also in closed form) represent the convection in velocity space due to the resolved pressure gradient and molecular diffusion, respectively. The last two terms are unclosed and denote convective effects in the velocity space due to SGS pressure gradient and SGS diffusion.

Alternatively, the conditional diffusion term in Eq. (15) can be represented as

$$-\frac{\partial}{\partial v_i}\left[\left\langle \frac{\partial \sigma_{ik}}{\partial x_k}\middle|\boldsymbol{v}\right\rangle_L P_L(\boldsymbol{v};\mathbf{x},t)\right]$$

$$= \nu\frac{\partial^2 P_L(\boldsymbol{v};\mathbf{x},t)}{\partial x_k \partial x_k} - \frac{\partial^2}{\partial v_i \partial v_j}\left[\left\langle \nu\frac{\partial u_i}{\partial x_k}\frac{\partial u_j}{\partial x_k}\middle|\boldsymbol{v}\right\rangle_L P_L(\boldsymbol{v};\mathbf{x},t)\right], \tag{16}$$

in which the second term on the right-hand side (rhs) involves the conditional expected dissipation. With this, the alternate form of the VFDF transport equation is

$$\frac{DP_L}{Dt} = -\frac{\partial}{\partial x_k}\left[(v_k - \langle u_k\rangle_L)P_L\right] + \frac{\partial\langle p\rangle_L}{\partial x_i}\frac{\partial P_L}{\partial v_i} + \nu\frac{\partial^2 P_L}{\partial x_k \partial x_k}$$

$$+\frac{\partial}{\partial v_i}\left[\left(\left\langle \frac{\partial p}{\partial x_i}\middle|\boldsymbol{v}\right\rangle_L - \frac{\partial\langle p\rangle_L}{\partial x_i}\right)P_L\right]$$

$$-\frac{\partial^2}{\partial v_i \partial v_j}\left[\left\langle \nu\frac{\partial u_i}{\partial x_k}\frac{\partial u_j}{\partial x_k}\middle|\mathbf{v}\right\rangle_L P_L\right]. \tag{17}$$

Equation (17) is another exact transport equation for the VFDF. The first term on the right-hand side represents the SGS convection of the VFDF in physical space and is closed. The second term corresponds to the convection in the velocity space due to the resolved pressure gradient. The third term represents molecular diffusion of the VFDF in physical space. The closure problem is associated with the last two terms.

C. Modeled VFDF transport equations

The generalized Langevin model (GLM)[27,32] is employed for closure of the VFDF transport equation. Here we introduce two modeled VFDF equations, which are denoted by "VFDF1" and "VFDF2." These are presented in order. To close Eq. (17), VFDF1 is

$$\frac{\partial}{\partial v_i}\left[\left(\left\langle \frac{\partial p}{\partial x_i}\middle|\boldsymbol{v}\right\rangle_L - \frac{\partial\langle p\rangle_L}{\partial x_i}\right)P_L\right]$$

$$-\frac{\partial^2}{\partial v_i \partial v_j}\left[\left\langle \nu\frac{\partial u_i}{\partial x_k}\frac{\partial u_j}{\partial x_k}\middle|\boldsymbol{v}\right\rangle_L P_L\right]$$

$$\approx -\frac{\partial}{\partial v_i}\left[G_{ij}(v_j - \langle u_j\rangle_L)P_L\right] + \frac{1}{2}C_0\varepsilon\frac{\partial^2 P_L}{\partial v_i \partial v_i}$$

$$+\nu\frac{\partial\langle u_i\rangle_L}{\partial x_k}\frac{\partial\langle u_j\rangle_L}{\partial x_k}\frac{\partial^2 P_L}{\partial v_i \partial v_j} + 2\nu\frac{\partial\langle u_i\rangle_L}{\partial x_k}\frac{\partial^2 P_L}{\partial x_k \partial v_i}. \tag{18}$$

To close Eq. (15), VFDF2 is

$$\frac{\partial}{\partial v_i}\left[\left(\left\langle \frac{\partial p}{\partial x_i}\middle|\boldsymbol{v}\right\rangle_L - \frac{\partial\langle p\rangle_L}{\partial x_i} - \left\langle \frac{\partial \sigma_{ik}}{\partial x_k}\middle|\boldsymbol{v}\right\rangle_L + \frac{\partial\langle \sigma_{ik}\rangle_L}{\partial x_k}\right)P_L\right]$$

$$\approx -\frac{\partial}{\partial v_i}\left[G_{ij}(v_j - \langle u_j\rangle_L)P_L\right] + \frac{1}{2}C_0\varepsilon\frac{\partial^2 P_L}{\partial v_i \partial v_i}. \tag{19}$$

Note that these models (i.e., the first two terms on the right-hand sides of Eqs. (18) and (19) are the same, but that they model slightly different quantities. With this closure, the two terms in G_{ij} and ε jointly represent the SGS pressure-strain and SGS dissipation. These are modeled as[11,26]

$$G_{ij} = -\omega\left(\frac{1}{2} + \frac{3}{4}C_0\right)\delta_{ij}, \quad \varepsilon = C_\varepsilon k^{3/2}/\Delta_L, \quad \omega = \varepsilon/k, \tag{20}$$

where ω is the SGS mixing frequency, Δ_L is the filter width, $k = \frac{1}{2}\tau_L(u_i, u_i)$ is the SGS kinetic energy, and $\varepsilon = \frac{1}{2}\varepsilon_{ii}$ is the SGS dissipation rate.

With the GLM, the two forms of the VFDF transport equation are

$$\frac{DP_L}{Dt} = -\frac{\partial}{\partial x_k}[(v_k - \langle u_k\rangle_L)P_L] + \frac{\partial\langle p\rangle_L}{\partial x_i}\frac{\partial P_L}{\partial v_i} + \nu\frac{\partial^2 P_L}{\partial x_k \partial x_k}$$

$$+ \nu\frac{\partial\langle u_i\rangle_L}{\partial x_k}\frac{\partial\langle u_j\rangle_L}{\partial x_k}\frac{\partial^2 P_L}{\partial v_i \partial v_j} + 2\nu\frac{\partial\langle u_i\rangle_L}{\partial x_k}\frac{\partial^2 P_L}{\partial x_k \partial v_i}$$

$$- \frac{\partial}{\partial v_i}[G_{ij}(v_j - \langle u_j\rangle_L)P_L] + \frac{1}{2}C_0\varepsilon\frac{\partial^2 P_L}{\partial v_i \partial v_i}, \tag{21}$$

for VFDF1, and

$$\frac{DP_L}{Dt} = -\frac{\partial}{\partial x_k}[(v_k - \langle u_k\rangle_L)P_L] + \frac{\partial\langle p\rangle_L}{\partial x_i}\frac{\partial P_L}{\partial v_i}$$

$$- \frac{\partial\langle\sigma_{ik}\rangle_L}{\partial x_k}\frac{\partial P_L}{\partial v_i} - \frac{\partial}{\partial v_i}[G_{ij}(v_j - \langle u_j\rangle_L)P_L]$$

$$+ \frac{1}{2}C_0\varepsilon\frac{\partial^2 P_L}{\partial v_i \partial v_i} \tag{22}$$

for VFDF2. Hereinafter, Eqs. (21) and (22) are referred to as "VFDF1" and "VFDF2," respectively. The difference between these two equations is in the different treatment of the closed viscous terms.

D. Transport equations for moments

The zeroth, first, and second moment equations corresponding to these two formulations are

for VFDF1:

$$\frac{\partial\langle u_i\rangle_L}{\partial x_i} = 0,$$

$$\frac{\partial\langle u_j\rangle_L}{\partial t} + \frac{\partial\langle u_i\rangle_L\langle u_j\rangle_L}{\partial x_i}$$

$$= -\frac{\partial\langle p\rangle_L}{\partial x_j} + \nu\frac{\partial^2\langle u_j\rangle_L}{\partial x_i \partial x_i} - \frac{\partial\tau_L(u_i, u_j)}{\partial x_i}, \tag{23}$$

$$\frac{\partial}{\partial t}[\tau_L(u_i, u_j)] + \frac{\partial}{\partial x_k}[\langle u_k\rangle_L\tau_L(u_i, u_j)]$$

$$= -\frac{\partial}{\partial x_k}\left[\tau_L(u_i, u_j, u_k) - \nu\frac{\partial}{\partial x_k}[\tau_L(u_i, u_j)]\right]$$

$$+ G_{ik}\tau_L(u_j, u_k) + G_{jk}\tau_L(u_i, u_k) - \tau_L(u_i, u_k)\frac{\partial\langle u_j\rangle_L}{\partial x_k}$$

$$- \tau_L(u_j, u_k)\frac{\partial\langle u_i\rangle_L}{\partial x_k} + C_0\varepsilon\delta_{ij}, \tag{24}$$

for VFDF2:

$$\frac{\partial\langle u_i\rangle_L}{\partial x_i} = 0,$$

$$\frac{\partial\langle u_j\rangle_L}{\partial t} + \frac{\partial\langle u_i\rangle_L\langle u_j\rangle_L}{\partial x_i}$$

$$= -\frac{\partial\langle p\rangle_L}{\partial x_j} + \nu\frac{\partial^2\langle u_j\rangle_L}{\partial x_i \partial x_i} - \frac{\partial\tau_L(u_i, u_j)}{\partial x_i}, \tag{25}$$

$$\frac{\partial}{\partial t}[\tau_L(u_i, u_j)] + \frac{\partial}{\partial x_k}[\langle u_k\rangle_L\tau_L(u_i, u_j)]$$

$$= -\frac{\partial}{\partial x_k}[\tau_L(u_i, u_j, u_k)] + G_{ik}\tau_L(u_j, u_k) + G_{jk}\tau_L(u_i, u_k)$$

$$- \tau_L(u_i, u_k)\frac{\partial\langle u_j\rangle_L}{\partial x_k} - \tau_L(u_j, u_k)\frac{\partial\langle u_i\rangle_L}{\partial x_k} + C_0\varepsilon\delta_{ij}. \tag{26}$$

It may be seen that the zeroth and first moment equations are identical (and exact); whereas the second central moment equations differ by the additional viscous term in VFDF1 [Eq. (24)]. A comparison of these modeled equations with Eq. (5) shows that the GLM model implies

$$-\Pi_{ij} - (\varepsilon_{ij} - \tfrac{2}{3}\varepsilon\delta_{ij}) = -C_1\omega[\tau_L(u_i, u_j) - \tfrac{2}{3}k\delta_{ij}],$$

$$C_1 = 1 + \tfrac{3}{2}C_0. \tag{27}$$

This is the same as the Rotta[33] model as shown by Pope.[34] There are two model constants in the VFDF equation. In RAS, typically[34,35] $C_\varepsilon \approx 1$, and $C_0 \approx 2.1$ ($C_1 = 4.15$). As shown in Refs. 27, 34 boundedness of the GLM coefficients $C_0 > 0$ guarantees that the SGS stress is realizable.

IV. EQUIVALENT STOCHASTIC SYSTEMS

The solution of the VFDF transport equation provides all the statistical information pertaining to the velocity vector. The most convenient means of solving this equation is via the Lagrangian Monte Carlo scheme. The basis of this scheme relies upon the principle of equivalent systems.[26,32] Two systems with different instantaneous behaviors may have identical statistics and satisfy the same PDF transport equation. In this context, the general diffusion process is considered via the following system of stochastic differential equations (SDEs):[26,31,36,37]

$$d\mathcal{X}_i(t) = D_i(\mathcal{X}(t), \mathcal{U}(t); t)dt + B(\mathcal{X}(t), \mathcal{U}(t); t)dW_i^x(t),$$

$$d\mathcal{U}_i(t) = M_i(\mathcal{X}(t), \mathcal{U}(t); t)dt + E(\mathcal{X}(t), \mathcal{U}(t); t)dW_i^v(t)$$

$$+ F_{ij}(\mathcal{X}(t), \mathcal{U}(t); t)dW_j^x(t), \tag{28}$$

where $\mathcal{X}_i$ and $\mathcal{U}_i$ are probabilistic representations of **x** and *u*, respectively. The coefficients D_i and M_i are the "drift" in the phase space of position and velocity, respectively. The terms B and E are the "diffusion" coefficients for physical and velocity spaces, respectively; and W_i^x and W_i^v denote independent Wiener–Lévy processes.[38] The tensor F_{ij} represents the dependency between the velocity and physical spaces. This term is needed to satisfy the Itô condition for

$B \neq 0$. A comparison of the Fokker–Planck equation of Eq. (28) with the modeled VFDF1 transport equation, Eq. (21) yields

$$M_i \equiv -\frac{\partial \langle p \rangle_L}{\partial x_i} + 2\nu \frac{\partial^2 \langle u_i \rangle_L}{\partial x_k \partial x_k} + G_{ij}(\mathcal{U}_j - \langle u_j \rangle_L), \quad D_i \equiv \mathcal{U}_i,$$

$$B \equiv \sqrt{2\nu}, \quad E \equiv \sqrt{C_0 \varepsilon}, \quad F_{ij} \equiv \sqrt{2\nu} \frac{\partial \langle u_i \rangle_L}{\partial x_j}. \quad (29)$$

Therefore, the proper SDEs which represent VFDF1 in the Lagrangian sense are

$$d\mathcal{X}_i(t) = \mathcal{U}_i(t)dt + \sqrt{2\nu} dW_i^x(t),$$

$$d\mathcal{U}_i(t) = \left[-\frac{\partial \langle p \rangle_L}{\partial x_i} + 2\nu \frac{\partial^2 \langle u_i \rangle_L}{\partial x_k \partial x_k} + G_{ij}(\mathcal{U}_j(t) - \langle u_j \rangle_L) \right] dt$$

$$+ \sqrt{C_0 \varepsilon} dW_i^v(t) + \sqrt{2\nu} \frac{\partial \langle u_i \rangle_L}{\partial x_j} dW_j^x(t). \quad (30)$$

This stochastic system is the same as that developed by Dreeben and Pope[29–31] for RAS.

For VFDF2, due to the absence of diffusion in physical space we must have $B = 0$. Therefore, the corresponding SDEs are

$$d\mathcal{X}_i(t) = \mathcal{U}_i(t)dt,$$

$$d\mathcal{U}_i(t) = \left[-\frac{\partial \langle p \rangle_L}{\partial x_i} + \frac{\partial \langle \sigma_{ik} \rangle_L}{\partial x_k} + G_{ij}(\mathcal{U}_j(t) - \langle u_j \rangle_L) \right] dt$$

$$+ \sqrt{C_0 \varepsilon} dW_i^v(t). \quad (31)$$

This system is the same as that suggested by Pope[26] and Haworth and Pope[27] for RAS.

The primary difference between the two formulations VFDF1 and VFDF2 is due to molecular effects in the spatial diffusion of the VFDF. This is explicitly included in the VFDF1 formulation and is also present in the corresponding second moment equation. This difference is expected to be important in flows where viscous effects are important; e.g., flow near solid boundaries.[29–31] Both of these formulation are considered in our numerical simulations as discussed below.

V. NUMERICAL SOLUTION PROCEDURE

Numerical solution of the modeled VFDF transport equation is obtained by a Lagrangian Monte Carlo procedure. The basis of this procedure is the same as that in RAS[39–41] and in previous LES/FDF.[6,8] But there are some subtle differences which are explained here. In the Lagrangian description, the VFDF is represented by an ensemble of N statistically identical Monte Carlo particles. Each of these particles carries information pertaining to its velocity $\mathbf{U}^{(n)}(t)$ and position $\mathbf{X}^{(n)}(t)$, $n = 1, 2, \dots N$. This information is updated via temporal integration of Eq. (28). The simplest means of performing this integration is via the Euler–Maruyamma approximation[42]

$$X_i^n(t_{k+1}) = X_i^n(t_k) + D_i^n(t_k)\Delta t + B^n(t_k)(\Delta t)^{1/2}\zeta_i^n(t_k),$$

$$U_i^n(t_{k+1}) = U_i^n(t_k) + M_i^n(t_k)\Delta t + E^n(t_k)(\Delta t)^{1/2}\xi_i^n(t_k)$$

$$+ F_{ij}^n(t_k)(\Delta t)^{1/2}\zeta_j^n(t_k), \quad (32)$$

where $D_i^n(t_k) = D_i(\mathbf{X}^{(n)}(t_k), \mathbf{U}^{(n)}(t_k); t)$, $B^{(n)}(t_k) = B(\mathbf{X}^{(n)}(t_k), \mathbf{U}^{(n)}(t_k); t), \dots$ and $\xi_i^n(t_k)$, $\zeta_j^n(t_k)$ are independent standardized Gaussian random variables. This formulation preserves the Markovian character of the diffusion processes[43,44] and facilitates affordable computations. Higher-order numerical schemes for solving Eq. (28) are available,[42] but one must be cautious in using them for LES.[6] Since the diffusion term in Eq. (28) strongly depends on the stochastic processes, the numerical scheme must be consistent with Itô–Gikhman[45,46] calculus. Equation (32) exhibits this property.

The statistics are evaluated by consideration of the ensemble of particles in a "finite volume" centered at a spatial location. This ensemble provides "one-time" statistics. This finite volume is characterized by a cubic box of length Δ_E. This is necessary as, with probability one, no particle will coincide with the point as considered.[32] Here, a cubic box of size Δ_E is used to construct the ensemble mean, variances and covariances of the velocity vector. These values are used in the finite difference LES solver of Eq. (4) as described below.

The SGS dissipation rate and the SGS mixing frequency as required in the solution of the VFDF are evaluated on the finite difference grid points and interpolated to the particle's location. Ideally, for reliable Eulerian statistics and minimum numerical dispersion, it is desired to have the size of the sample domain infinitesimally small (i.e., $\Delta_E \rightarrow 0$) and the number of particles within this domain infinitely large. That is

$$P_L(\boldsymbol{v}; \mathbf{x}, t) \xleftarrow[\substack{N_E \rightarrow \infty \\ \Delta_E \rightarrow 0}]{} \mathcal{P}_{N_E}(\boldsymbol{v}; \mathbf{x}, t) \equiv \frac{1}{N_E} \sum_{n \in \Delta_E} \delta(\boldsymbol{v} - \boldsymbol{u}^{(n)}),$$

$$(33)$$

where $\mathcal{P}_{N_E}$ is the Eulerian PDF constructed from the particle ensemble, $n \in \Delta_E$ denotes the particles contained in an ensemble box of length Δ_E centered at $\mathbf{x}$; and N_E is the total number of particles within the box. With a finite number of particles, obviously a larger Δ_E is needed. This compromise between the statistical accuracy and dispersive accuracy implies that the optimum magnitude of Δ_E cannot, in general, be specified *a priori*.[11,26] This does not diminish the capability of the procedure, but exemplifies the importance of the parameters governing the statistics.

To provide an estimate of the proper Δ_E size, a "point estimator" procedure is considered. With this procedure, the mean values (the first moments of the VFDF) are evaluated by ensemble averaging, and spatial variations of these mean values within the box are ignored. With the discrete representation [Eq. (32)], the first two moments in this procedure are evaluated via

TABLE I. Recapitulation of the VFDF solution procedures.

	Finite difference variables	Particle solver variables	Particle statistics used by the finite difference solver	Finite difference variables used by particle solver	Redundant quantities
VFDF 1	$\langle u_i \rangle_L$	X_i	$\tau_L(u_i, u_j)$	$\langle u_i \rangle_L, \dfrac{\partial \langle p \rangle_L}{\partial x_i}$	$\langle u_i \rangle_L$
	$\langle p \rangle_L$	U_i		$\dfrac{\partial \langle u_i \rangle_L}{\partial x_k}, \dfrac{\partial^2 \langle u_i \rangle_L}{\partial x_k \partial x_k}$	
VFDF 2	$\langle u_i \rangle_L$	X_i	$\tau_L(u_i, u_j)$	$\langle u_i \rangle_L, \dfrac{\partial \langle p \rangle_L}{\partial x_i}$	$\langle u_i \rangle_L$
	$\langle p \rangle_L$	U_i		$\dfrac{\partial^2 \langle u_i \rangle_L}{\partial x_k \partial x_k}$	
LES-FD	$\langle u_i \rangle_L, \langle p \rangle_L$	X_i	$\tau_L(u_i, u_j, u_k)$	$\langle u_i \rangle_L, \dfrac{\partial \langle p \rangle_L}{\partial x_i}$	$\langle u_i \rangle_L$
	$\tau_L(u_i, u_j)$	U_i		$\dfrac{\partial^2 \langle u_i \rangle_L}{\partial x_k \partial x_k}$	$\tau_L(u_i, u_j)$

$$\langle u_i \rangle_L \xleftarrow[\substack{N_E \to \infty \\ \Delta_E \to 0}]{} \frac{1}{N_E} \sum_{n \in \Delta_E} U_i^{(n)} \equiv \langle U_i \rangle_E,$$

$$\tau_L(u_i, u_j) \xleftarrow[\substack{N_E \to \infty \\ \Delta_E \to 0}]{} \frac{1}{N_E - 1} \sum_{n \in \Delta_E} (U_i^{(n)} - \langle U_i \rangle_E)(U_j^{(n)} - \langle U_j \rangle_E).$$

(34)

The point estimator is obviously subject to both statistical errors and dispersive errors for $\Delta_E \neq 0$.

To determine the pressure field, the "mean-field solver" is based on the "compact parameter" finite difference scheme of Carpenter.[47] This is a variant of the McCormack[48] scheme in which fourth-order compact differences are used to approximate the spatial derivatives, and a second-order symmetric predictor-corrector sequence is employed for time discretization. The numerical algorithm is a hyperbolic solver which considers a fully compressible flow. Here, the simulations are conducted with a low Mach number ($M \leqslant 0.3$) to minimize compressibility effects. All the finite difference operations are conducted on fixed and equally sized grid points. The transfer of information from these points to the location of the Lagrangian particles is conducted via interpolation. A second-order (bilinear) interpolation scheme is used for this purpose. The results of previous work indicate no significant improvements with the use of higher order interpolation schemes.[6]

The mean-field solver also determines the filtered velocity field. That is, there is a "redundancy" in the determination of the first filtered moments as both the finite difference and the Monte Carlo procedures provides the solution of this field. This redundancy is actually very useful in monitoring the accuracy of the simulated results. Detailed discussions pertaining to this issue are provided in Refs. 8, 39–41.

To establish the consistency of the VFDF solver, another LES is also conducted in which the modeled transport equations for the filtered velocity and the generalized SGS stresses are solved strictly via the finite difference scheme. These simulations are referred to as LES-FD and are only applied for the case corresponding to VFDF2. That is, Eqs. (25) and (26) are considered. Since the SGS transport terms $\tau_L(u_i, u_j, u_k)$ are unclosed in Eq. (26), the values corresponding to these terms are taken from the Monte Carlo solver and substituted in the SGS stress transport equations. The attributes of all of the scheme are summarized in Table I, with further discussions in Refs. 6, 39–41.

VI. RESULTS

A. Flows simulated

Simulations are conducted of a two-dimensional (2D) planar jet, and a 3D temporally developing mixing layer. The jet flow simulations are conducted primarily for establishing the consistency of the Lagrangian Monte Carlo solver. For this purpose, 2D simulations are sufficient. To analyze the overall performance of the VFDF and to demonstrate its full capabilities and drawbacks, 3D simulations are required.

In the planar jet, a fluid issues from a jet of width D into a co-flowing stream with a lower velocity. The size of the domain in the streamwise (x) and cross-stream (y) directions are $0 \leqslant x \leqslant 14D$ and $-3.5D \leqslant y \leqslant 3.5D$. The ratio of the co-flowing stream velocity to that of the jet at the inlet is kept fixed at 0.5. A double-hyperbolic tangent profile is utilized to assign the velocity distribution at the inlet plane. The formation of the large scale coherent structures are expedited by imposing low amplitude perturbations at the inlet. In the finite difference simulations, the characteristic boundary condition procedure of Ref. 49 is used at the inlet, free-shear boundary conditions are used at the free-streams and the pressure boundary condition of Ref. 50 is used at the outflow.

The temporal mixing layer consists of two parallel streams traveling in opposite directions with the same speed.[51–53] A hyperbolic tangent profile is utilized to assign the velocity distribution at the initial time. The simulations are conducted for a cubic box, $0 \leqslant x \leqslant L$, $-L/2 \leqslant y \leqslant L/2$, $0 \leqslant z \leqslant L$, where x, y, and z denote the streamwise, the cross-stream and the spanwise directions, respectively; and the length, L is specified such that $L = 2^{N_P} \lambda_u$, where N_P is the

desired number of successive vortex pairings and λ_u is the wavelength of the most unstable mode corresponding to the mean streamwise velocity profile imposed at the initial time. The flowfield is parameterized in a procedure somewhat similar to that by Vreman *et al.*[20] The formation of the large-scale structures are expedited through eigenfunction based initial perturbations.[54,55] This includes two-dimensional[20,52,56] and three-dimensional[52,57] perturbations with a random phase shift between the 3D modes. This results in the formation of two successive vortex pairings and strong three-dimensionality.

The flow variables are normalized with respect to selected reference quantities. In the jet flow, the jet exit velocity, and the jet width are the reference scales. In the temporal mixing layer, the reference length is the half initial vorticity thickness, $L_r = \delta_v(t=0)/2$ ($\delta_v = \Delta U / |\partial \langle u_1 \rangle_L / \partial y|_{max}$, where $\overline{\langle u_1 \rangle_L}$ is the Reynolds averaged value of the filtered streamwise velocity and ΔU is the velocity difference across the layer). The reference velocity is $U_r = \Delta U / 2$.

B. Numerical specifications

All finite difference simulations are conducted on equally spaced grid points with grid spacings $\Delta x = \Delta y = \Delta z$ (for 3D) $= \Delta$. The resolution for LES of the planar jet consists of 201×101 grid points. This allows simulations with a Reynolds number $Re = U_r D / v = 14,000$. The simulations of the temporal mixing layer are conducted on 193^3 and 33^3 points for DNS and LES, respectively. This allows simulations with $Re = U_r L_r / v = 50$.

To filter the DNS data, a top-hat function[21] of the form below is used

$$G(\mathbf{x}' - \mathbf{x}) = \prod_{i=1}^{N_D} \tilde{G}(x_i' - x_i),$$

$$\tilde{G}(x_i' - x_i) = \begin{cases} \dfrac{1}{\Delta_L} & |x_i' - x_i| \leq \dfrac{\Delta_L}{2} \\ 0 & |x_i' - x_i| > \dfrac{\Delta_L}{2} \end{cases}, \tag{35}$$

in which N_D denotes the number of dimensions, and $\Delta_L = 2\Delta$.[58] No attempt is made to investigate the sensitivity of the results to the filter function[24] or the size of the filter.[59]

For VFDF simulations of the temporal mixing layer, the Monte Carlo particles are initially distributed throughout the computational region. For the jet flow, the particles are supplied in the inlet region $-1.75D \leq y \leq 1.75D$. As the particles convect downstream, this zone distorts as it conforms to the flow as determined by the hydrodynamic field. The simulation results are monitored to ensure the particles fully encompass and extend well beyond regions of nonzero vorticity with an approximately uniform particle number density. All simulations are performed with a uniform "weight"[26] of the Monte Carlo particles. In the temporal mixing layer, due to flow periodicity in the streamwise and spanwise directions, if the particle leaves the domain at one of these boundaries new particles are introduced at the other boundary with the same compositional values. In the cross-

stream directions, the free-slip boundary condition is satisfied by the mirror-reflection of the particles leaving through these boundaries. In the planar jet, new particles are introduced through the inlet boundary at a rate proportional to the local flow velocity and with a velocity makeup dependent on the cross-stream direction only. When the particles leave the computational domain at the outflow, they are no longer tracked. The density of the Monte Carlo particles is determined by the average number of particles N_E within the ensemble domain of size $\Delta_E \times \Delta_E (\times \Delta_E)$. The effects of both of these parameters are assessed to ensure the consistency and the statistical accuracy of the VFDF simulations.

All results are analyzed both "instantaneously" and "statistically." In the former, the instantaneous contours (snap-shots) and scatter plots of the variables of interest are analyzed. In the latter, the "Reynolds-averaged" statistics constructed from the instantaneous data are considered. In the spatially developing flows this averaging procedure is conducted via sampling in time. In the temporal mixing layer, the statistics are constructed by spatial averaging over the x-z plane of statistical homogeneity. All Reynolds averaged results are denoted by an overbar.

C. Consistency and convergence assessments

The objective of this section is to demonstrate the consistency of the VFDF formulation and the convergence of its Monte Carlo simulation procedure. For this purpose, the results via VFDF and LES-FD are compared against each other. Since the accuracy of the finite difference procedure is well-established (at least for the first-order filtered quantities), such a comparative assessment provides a good means of assessing the performance of the Monte Carlo solution of the VFDF. To do so, the statistical results obtained from the Monte Carlo simulations of Eq. (31) are compared with the finite difference solution of Eqs. (25) and (26). Also, no attempt is made to determine the appropriate values of the model constants; the values suggested in the literature are adopted[34] $C_0 = 2.1 (C_1 = 4.15)$ and $C_\varepsilon = 1$.

In Fig. 1, the instantaneous contour plots of the vorticity are shown as determined by (a) VFDF2 and (b) LES-FD. This figure provides a simple visual demonstration of the consistency of the VFDF2. Scatter plots of $\langle u \rangle_L$ vs $\langle v \rangle_L$ are presented in Fig. 2. The correlation and regression coefficients (denoted, respectively, by ρ and r on these figures) are insensitive to Δ_E. Figures 3 and 4 show the Reynolds averaged values of the streamwise velocity and several components of the SGS stress tensor for several values of Δ_E, with $N_E = 40$ kept fixed. It is observed that the first filtered moments as obtained by VFDF agree very well with those via LES-FD even for large Δ_E values. However, smaller Δ_E values are required for convergence of the VFDF predicted SGS stresses to those by LES-FD. The relative difference between the L_2 norms of all of the components of the SGS tensor as a function of $(\Delta_E / \Delta)^2$ is presented in Fig. 5. Extrapolation to $\Delta_E = 0$ shows that the "error" goes to zero as $\Delta_E \rightarrow 0$.

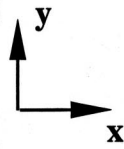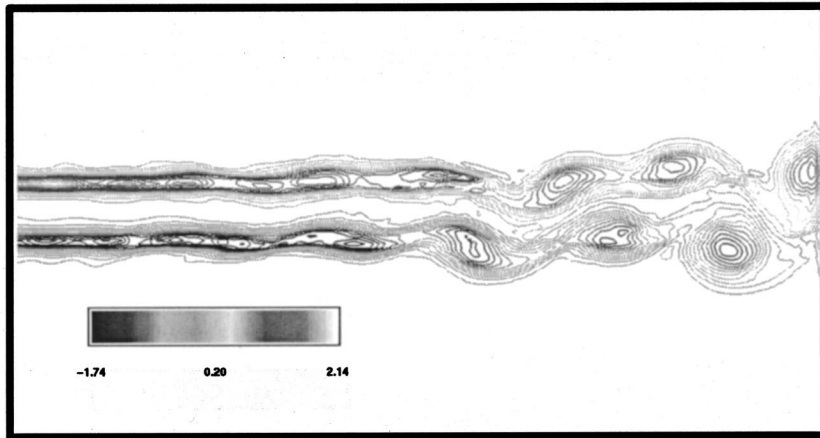The influence of N_E on the first two moments is shown

(a)
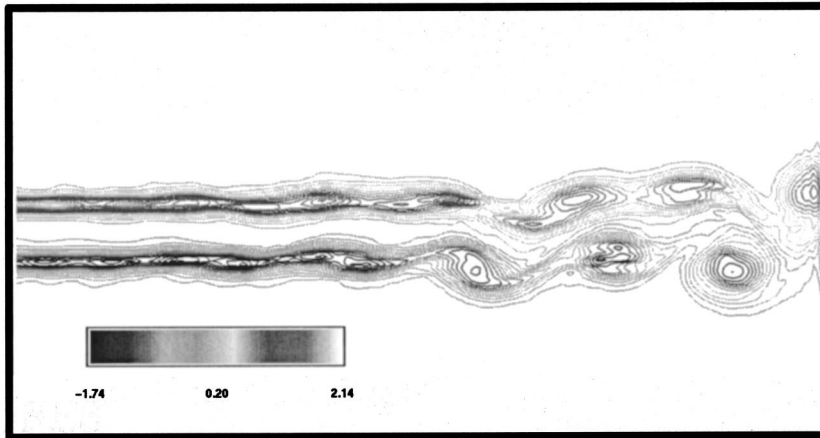
(b)

FIG. 1. Plot of the vorticity field contours, (a) VFDF2, (b) LES-FD. $\Delta_E = \Delta$, $N_E = 40$.

in Figs. 6 and 7. It is observed that N_E does not have a significant influence on the first moments, but does slightly influence the second moments. In all the cases considered, $N_E \geqslant 40$ yields reliable predictions, consistent with previous consistency and convergence assessments of the scalar FDF.[6,8] All the subsequent simulations are conducted with $\Delta_E = \Delta/2$ and $N_E = 40$.

D. Comparative assessments of the VFDF

The objective of this section is to analyze some of the characteristics of the VFDF via comparative assessments against DNS data. This assessment is done via both *a priori* and *a posteriori* analyses. In the former, the DNS results are used to determine the range of the empirical constants appearing in the VFDF sub-closures. In the latter, the final results as predicted by the VFDF are directly compared with those obtained by DNS. The procedure is similar to that in Ref. 20 and considers the 3D temporal mixing layer.

In addition to VFDF, three other LES are conducted with (1) no SGS model, (2) the Smagorinsky[16,60] SGS closure, and (3) the dynamic Smagorinsky[17–19] model. In the case with no model, the contribution of the SGS is completely ignored, i.e., $\tau_L(u_i, u_j) = 0$. In this case, the numerical errors amount to an implied model. But as indicated in Ref. 20 this

case is included to provide a point of reference for the other closures. The Smagorinsky model is[16,61]

$$\tau_L(u_i, u_j) - \tfrac{2}{3} k \delta_{ij} = -2 \nu_t S_{ij},$$

$$S_{ij} = \frac{1}{2} \left(\frac{\partial \langle u_i \rangle_L}{\partial x_j} + \frac{\partial \langle u_j \rangle_L}{\partial x_i} \right),$$ (36)

$$\nu_t = C_\nu \Delta_L^2 S.$$

$C_\nu = \sqrt{2}\, 0.17^2 \approx 0.04$, $S = \sqrt{S_{ij} S_{ij}}$ and Δ_L is the characteristic length of the filter. This model considers the anisotropic part of the SGS stress tensor $a_{ij} = \tau_L(u_i, u_j) - \tfrac{2}{3} k \delta_{ij}$. The isotropic components are absorbed in the pressure field. The dynamic version of the Smagorinsky model provides a means of approximating C_ν as suggested in Refs. 17–19. The procedure for the implementation of this model in the 3D temporal mixing layer LES is described by Vreman;[20] thus it is not repeated here. (See Refs. 11, 23, 62, and 63 for recent reviews on SGS closure strategy.)

In addition to the resolved velocity field, the primary integral statistical quantities considered for comparative assessments are
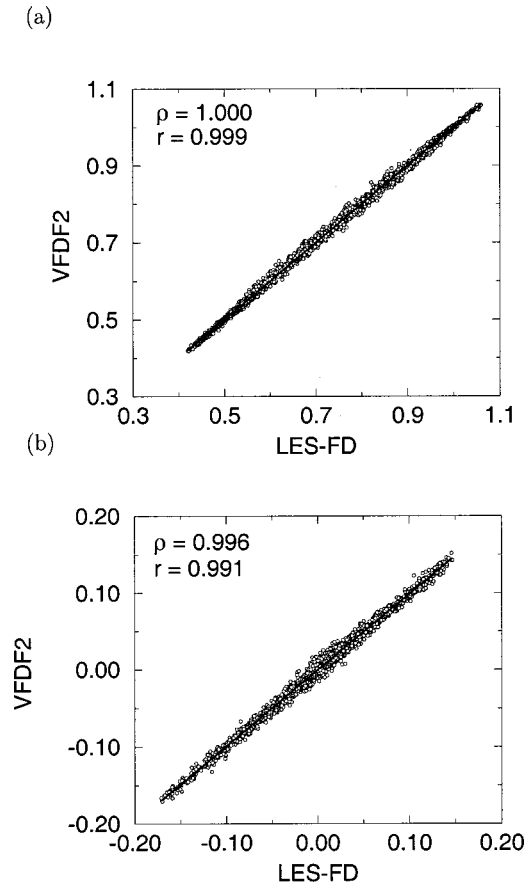
(a)

(b)

FIG. 2. Scatter plots of the filtered velocity field as obtained via VFDF2 vs LES-FD. (a), $\langle u \rangle_L$; (b), $\langle v \rangle_L$. $\Delta_E = \Delta$, $N_E = 40$.

$$E_f = \int \tfrac{1}{2} \langle u_i \rangle_L \langle u_i \rangle_L \mathbf{dx}, \qquad (37)$$

$$P_k = \int p_k \mathbf{dx}, \quad \text{with} \quad p_k = -\tau_L(u_i, u_j) \frac{\partial \langle u_i \rangle_L}{\partial x_j},$$

$$E_\nu = \int \varepsilon_\nu \mathbf{dx}, \quad \text{with} \quad \varepsilon_v = \nu \frac{\partial \langle u_i \rangle_L}{\partial x_k} \left(\frac{\partial \langle u_i \rangle_L}{\partial x_k} + \frac{\partial \langle u_k \rangle_L}{\partial x_i} \right), \qquad (38)$$

$$B_k = \int \min(0, p_k) \mathbf{dx}.$$

E_f is the kinetic energy of the resolved field, ε_v represents the viscous molecular dissipation rate directly from the filtered field, P_k is the production rate of the SGS kinetic energy (or the rate of energy transfer from the resolved filtered motion to the SGS motion), and B_k is the total backscatter.[64-66] The resolved molecular dissipation rate is always positive (by definition), but the production rate of the SGS kinetic energy can be locally negative. This backscatter is not represented in the Smagorinsky model. The dynamic model is potentially capable of accounting for it, but at the expense of causing numerical instabilities. In the implementation of the dynamic model used here, backscatter is avoided by averaging the numerator and denominator of the expression determining C_v (Refs. 19 and 20) over the homogeneous directions. If negative values are still present, they

(a)

(b)

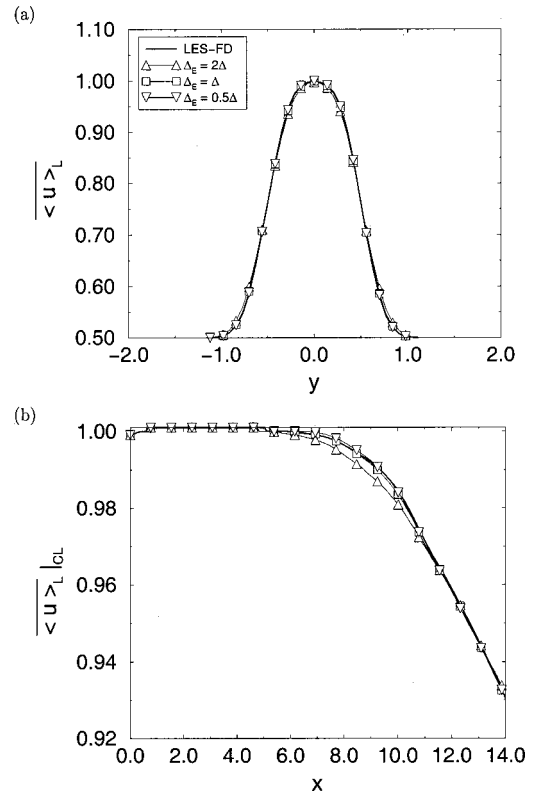
FIG. 3. Reynolds averaged values of the filtered streamwise velocity. (a) Cross-stream variations at $x=7$, (b) streamwise variation at $y=0$ (centerline). $N_E = 40$.

are set equal to zero.[20,63] The "resolved" components of the Reynolds-averaged stress tensor are denoted by $\overline{R_{ij}}$ where $R_{ij} = (\langle u_i \rangle_L - \overline{\langle u_i \rangle_L})(\langle u_j \rangle_L - \overline{\langle u_j \rangle_L})$. The "total" Reynolds stresses are denoted by $\overline{r_{ij}}$ where $r_{ij} = (u_i - \overline{u_i})(u_j - \overline{u_j})$. These are approximated by $\overline{r_{ij}} \approx \overline{R_{ij}} + \overline{\tau_L(u_i, u_j)}$.[20,67,68] In DNS, the total stresses are evaluated directly and the results indicate that $\overline{R_{ij}} + \overline{\tau_L(u_i, u_j)}$ does indeed approximate $\overline{r_{ij}}$ with a maximum error of less than 10%.

Figure 8 shows the distribution of the particle number density within the whole computational domain. Assuring an approximately uniform distribution, the values of the moments within local ensembles are compared with those of filtered DNS data. These DNS data are transposed from the original high resolution 193^3 points to the low resolution of 33^3 points, and then are compared with LES results on these coarse points.

The DNS data are also used to make *a priori* estimates of the model constants. The primary terms which require closure are the SGS dissipation and the velocity-pressure scrambling tensors. The model equation [Eq. (20)] involving C_ε is in a scalar form. For an estimate of C_1 (thus C_0), we consider the following norm of the corresponding closure [Eq. (27)]

$$\| -\Pi_{ij} - (\varepsilon_{ij} - \tfrac{2}{3} \varepsilon \delta_{ij}) \| \approx C_1 \omega \| \tau_L(u_i, u_j) - \tfrac{2}{3} k \delta_{ij} \|, \qquad (39)$$

where $\| W_{ij} \| = \sqrt{W_{ji} W_{ij}}$. To estimate the coefficients, a linear regression is performed on all the data points at each computational time step. The optimized constants as obtained in this way are denoted by $\tilde{C}_\varepsilon$ and $\tilde{C}_1$. This procedure is also
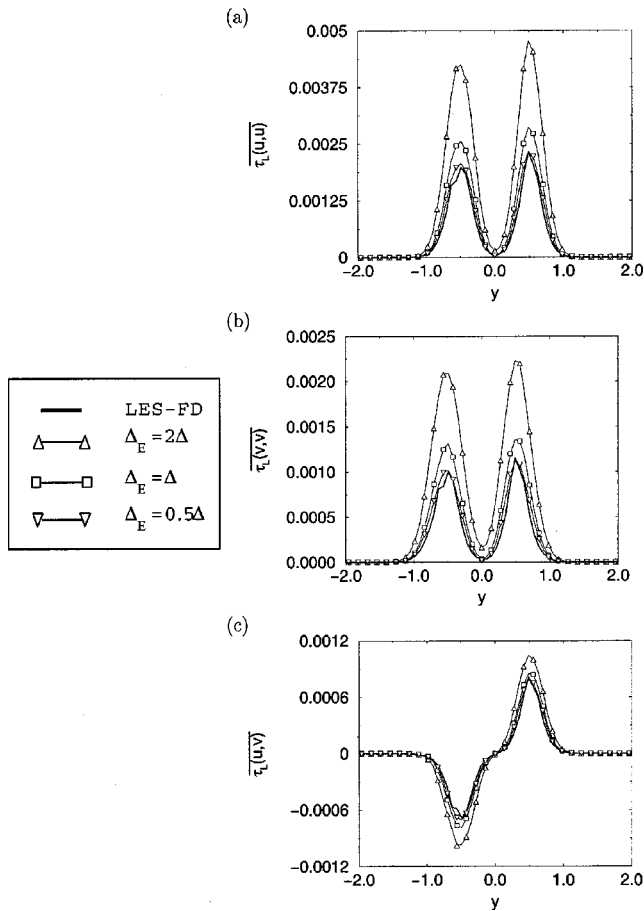
FIG. 4. Cross-stream variations of the Reynolds averaged values of some of the components of the SGS stress tensor at $x=7$ with $N_E=40$. The LES-FD results are obtained with $\Delta_E=0.5\Delta$, $N_E=40$.

FIG. 5. Percentage of the relative difference between the L_2 norms of the stresses as a function of Δ_E/Δ. (a) $x=2.8$, (b) $x=7$, (c) $x=11.2$.

followed for the Reynolds averaged data, with the optimized models obtained in this way denoted by $\overline{C_\varepsilon}$ and $\overline{C_1}$. The temporal variations of these estimated values are shown in Fig. 9. The nonuniformity of the coefficients indicates the "nonuniversality" of the models. This is expected as the flow evolves from an initially smooth laminar state to a strong three-dimensional state (at $t\approx 40$) before the action of the small scales becomes significant. The closures as adopted are not fully suitable for application in all of these flow regions. Nevertheless, Fig. 9 indicates that the values for these coefficients as suggested in RAS, i.e., $C_1\approx 4.15$, $C_\varepsilon\approx 1$ are reasonable, at least within the turbulent regime. The influences of these parameters are further investigated via *a posteriori* analysis of the results as discussed below.

Figures 10 and 11 show the contours of the spanwise and the streamwise components of the vorticity field, respectively, at time $t=80$. By this time, the flow has gone through several pairings and exhibits strong 3D effects. This is evident by the formation of large scale spanwise rollers with presence of counter-rotating streamwise vortex pairs in all the simulations. The results via the no-model indicate too many small-scale structures which clearly are not captured accurately on the coarse grid. The amount of SGS diffusion with the Smagorinsky model is very significant at initial times. Due to this dissipative characteristics of the model, the
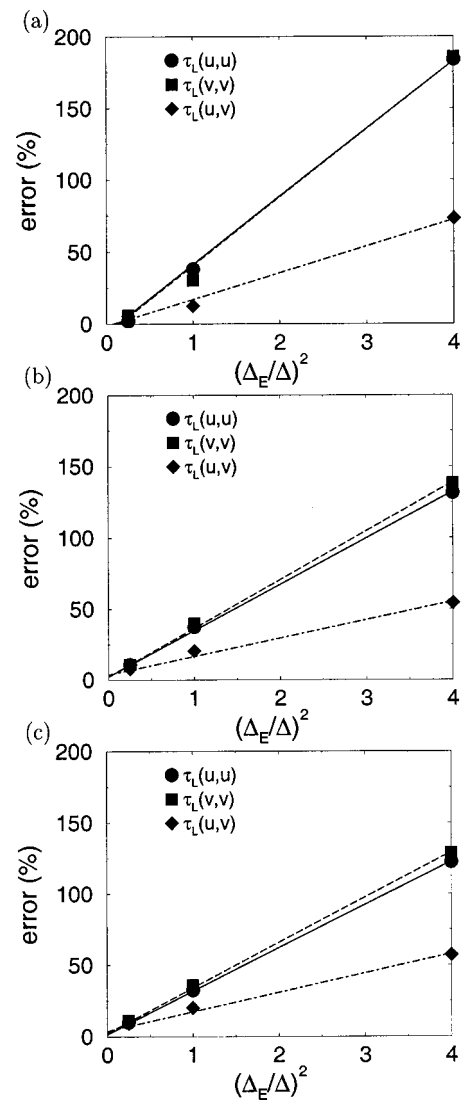
predicted results are too smooth and only contain the large scale structures. The vortical structures as depicted by the dynamic Smagorinsky and the VFDF are very similar and predict the DNS results better than the other two models. The results obtained by VFDF1 and VFDF2 are virtually indistinguishable from each other. This is expected, due to the lack of importance of molecular effects in this free shear flow.

The Reynolds averaged values of the streamwise velocity and the temporal variations of the momentum thickness

$$\delta_m(t)\frac{1}{4}=\int_{-L/2}^{L/2}(1-\overline{\langle u\rangle_L})(1+\overline{\langle u\rangle_L})dy, \qquad (40)$$

are shown in Figs. 12 and 13, respectively. In Fig. 12 the Reynolds averaged values of both filtered and unfiltered DNS data are considered and are shown to be essentially equivalent. Therefore, the latter are not shown in subsequent figures. The dissipative nature of the Smagorinsky model at initial times resulting in a slow growth of the layer is shown. Several values of the model parameters (C_0, C_ε) are consid-
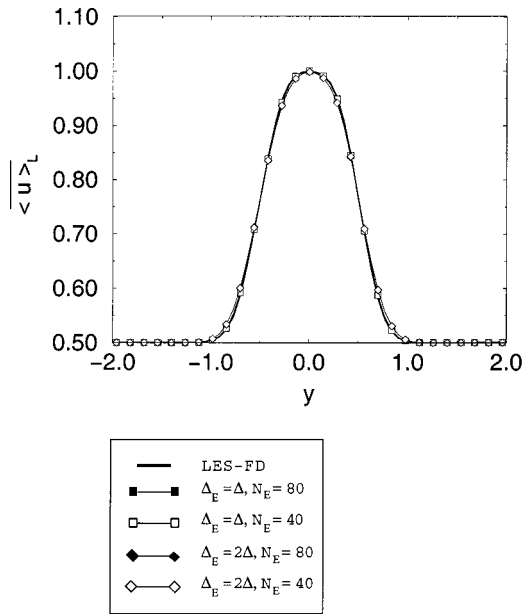
FIG. 6. Cross-stream variations of the Reynolds averaged values of the filtered streamwise velocity at $x=7$. The LES-FD results are obtained with $\Delta_E=0.5\Delta$, $N_E=40$.
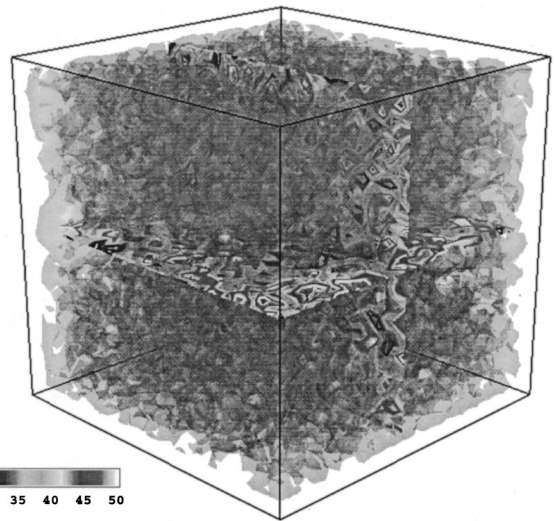

FIG. 8. Particle number density in VFDF2 simulation at $t=60$. The isosurface corresponds to $N_E=40$ set as initial conditions. $C_0=2.1$, $C_\varepsilon=1$.
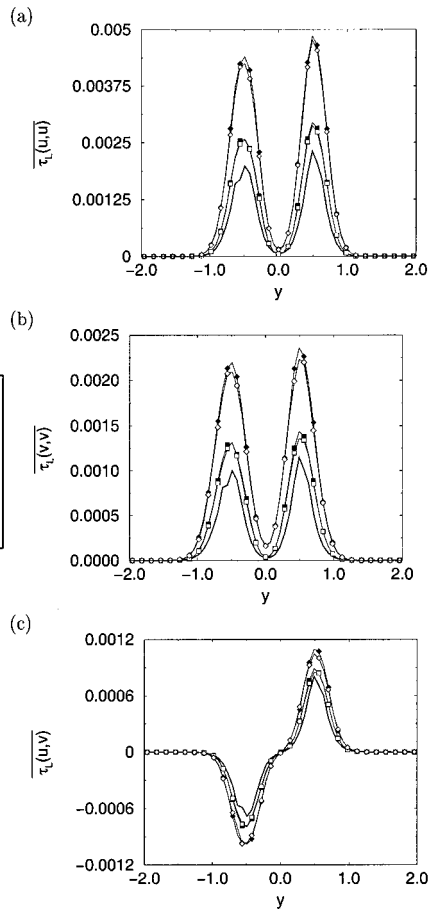
ered in the VFDF simulations. It is observed that as the magnitude of C_ε decreases, the initial rate of the layer's spread is higher. With the exception of the case with $C_\varepsilon=0.5$ and the Smagorinsky model, all the other VFDF cases, the dynamic Smagorinsky and the no-model yield a similar rate of layer's growth at late times.

The temporal variations of the resolved kinetic energy and all of the terms defined in Eq. (38) are shown in Fig. 14.

FIG. 7. Cross-stream variations of the Reynolds averaged values of some of the components of the SGS stress tensor at $x=7$. The LES-FD results are obtained with $\Delta_E=0.5\Delta$, $N_E=40$.
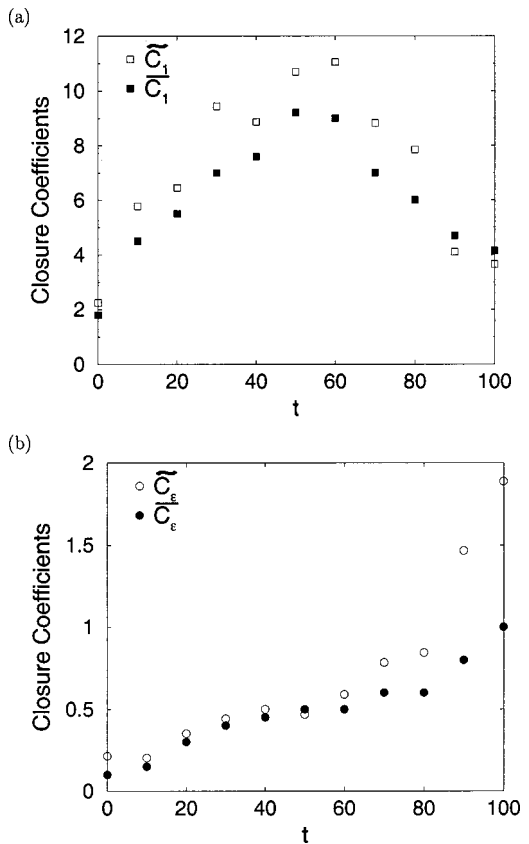

FIG. 9. Time variation of the model coefficients as obtained from *a priori* analysis of the DNS data.
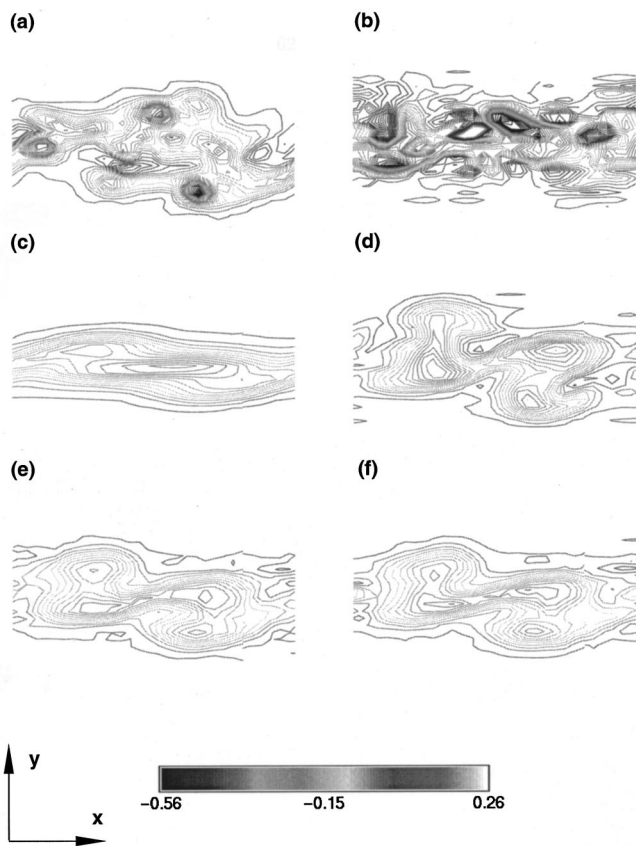
FIG. 10. Contour plots of the spanwise component of the vorticity at $z = 0.75L/L_r$, $t = 80$. (a) Filtered DNS, (b) no model, (c), Smagorinsky model, (d) dynamic Smagorinsky model, (e) VFDF2, $C_0 = 2.1$, $C_\varepsilon = 1$, (f) VFDF1, $C_0 = 2.1$, $C_\varepsilon = 1$.
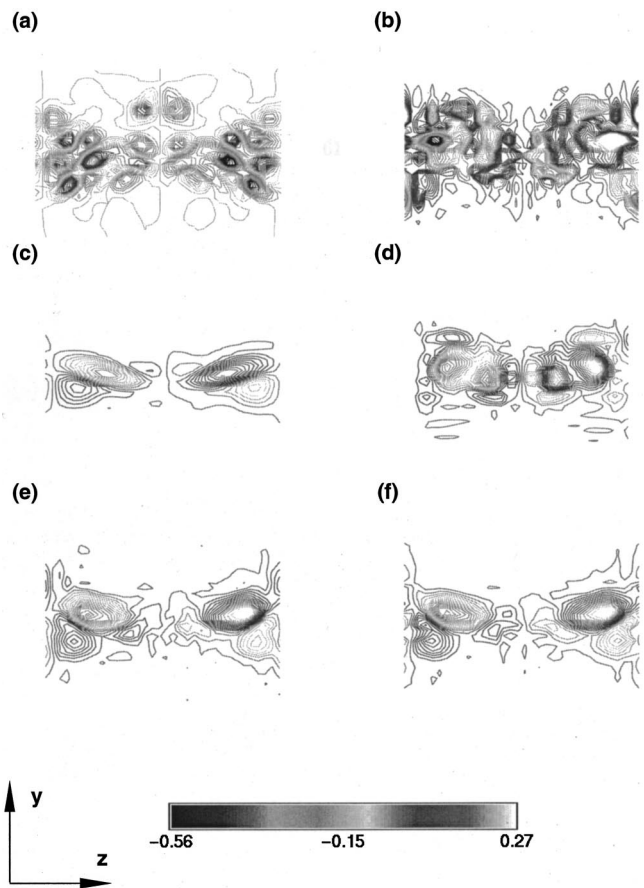

FIG. 11. Contour plots of the streamwise component of the vorticity vector at $x = 0.25L/L_r$, $t = 80$. (a) Filtered DNS, (b) no model, (c) Smagorinsky model, (d) dynamic Smagorinsky model, (e) VFDF2, $C_0 = 2.1$, $C_\varepsilon = 1$, (f) VFDF1, $C_0 = 2.1$, $C_\varepsilon = 1$.

The overall features displayed in this figure are similar to those reported by Vreman *et al.*[20] for the no model, the Smagorinsky model and the dynamic Smagorinsky model. The initial rate of decay of the resolved kinetic energy for the Smagorinsky model is the highest. This is due to the excessive production of the SGS kinetic energy by this model in the transitional region, and explains the reason for the lack of small scales in the vortical structures as discussed before. For all the other models the initial rate of decrease of the resolved kinetic energy is small and increases as the flow develops. The trend portrayed by DNS results is best captured by the VFDF simulations. For the no model case the only means of dissipation of the resolved kinetic energy is through molecular action and numerical dissipation which become significant at later stages due to presence of a large amount of small scales. In this case, the amount of numerical dissipation is the highest. For all the other closures, the productions rate of the SGS kinetic energy is larger than the molecular dissipation as the flow develops. The dynamic Smagorinsky and the no-model simulations predict the same initial rate of decay for the resolved kinetic energy. This is due to low initial values of P_k predicted by the dynamic Smagorinsky model. After $t = 40$ the amount of P_k as predicted by the dynamic model is more than that of molecular dissipation by the no-model. Thus the rate of decay of the resolved kinetic energy becomes higher for the dynamic

model and is closer to that obtained by DNS.

With the exception of the no-model case, all the simulations predict similar trends for the molecular dissipation. The magnitude of this dissipation as predicted by VFDF changes slightly with the variation of the model parameter. The production rate of the SGS kinetic energy depends more strongly on the model coefficients; as C_ε decreases, the peak
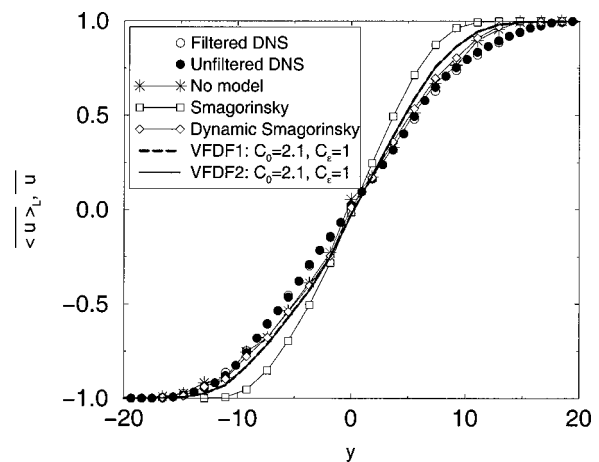

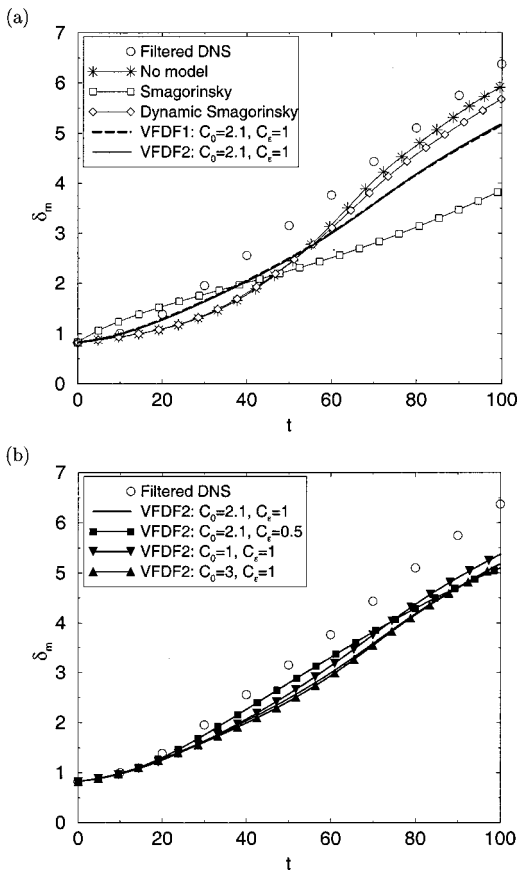FIG. 12. Cross-stream variations of the Reynolds averaged values of the streamwise velocity at $t = 70$.

FIG. 13. Temporal variations of the momentum thickness.

FIG. 15. Cross-stream variations of some of the components of $\overline{a_{ij}}$ at $t = 60$.

magnitude of P_k is larger. The Smagorinsky model does not adequately predict P_k, and the dynamic model yields better predictions at long times. The overall trends are best predicted by VFDF. The same is true in capturing the backscatter phenomenon. By design, the backscatter is identically zero in the Smagorinsky and the dynamic Smagorinsky model. But VFDF is capable of capturing it, and its extent is
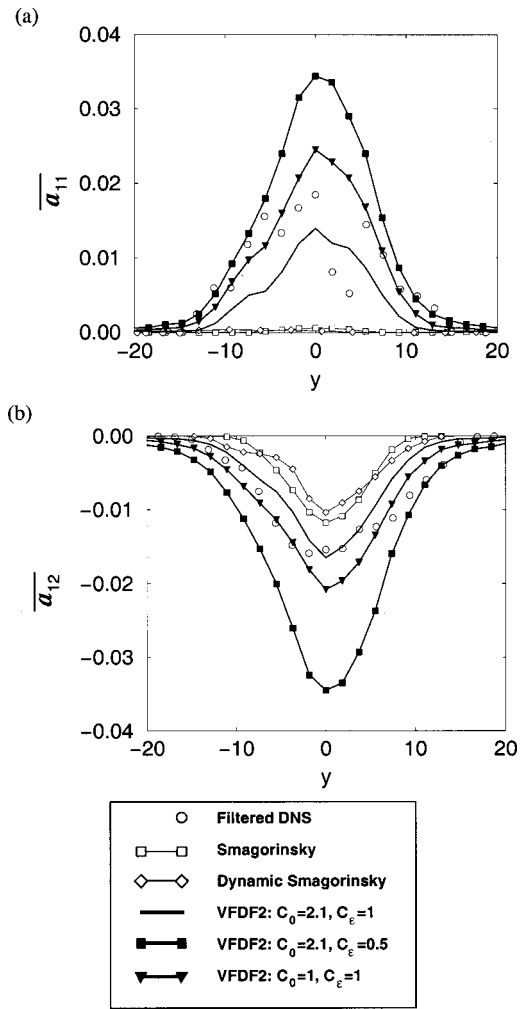
controlled by the model parameters. In this regard it is important to note that there are no numerical instability problems in the VFDF solver for negative B_k values. However, the amount of predicted backscatter is less than that of
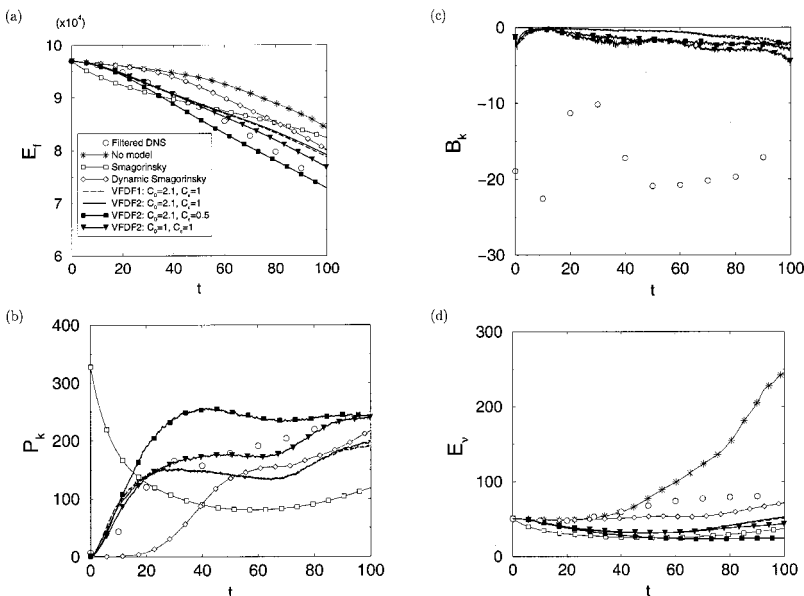

FIG. 14. Temporal variations of (a) total resolved kinetic energy, (b) SGS kinetic energy production rate, (c) total backscatter, (d) total resolved dissipation.
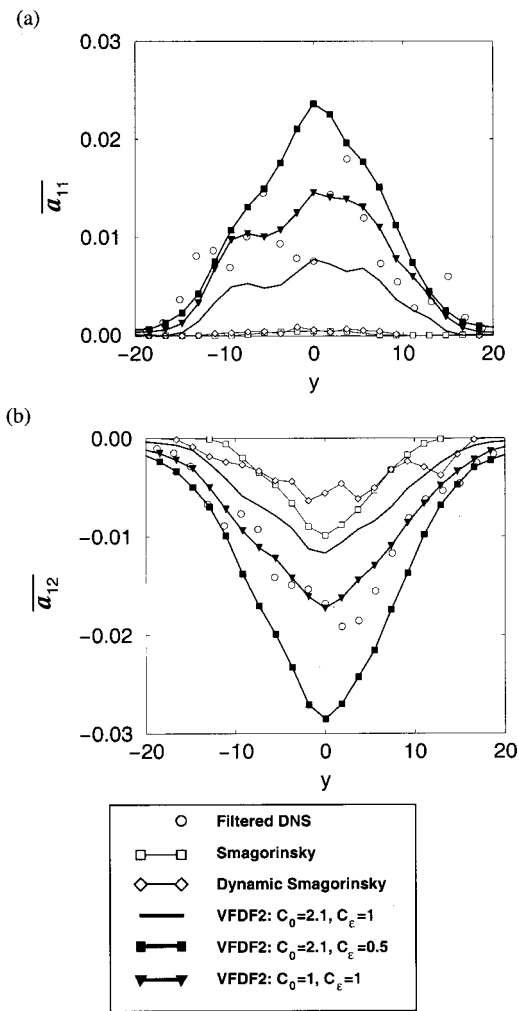
FIG. 16. Cross-stream variations of some of the components of $\overline{a_{ij}}$ at $t = 80$.

FIG. 17. Cross-stream variations of some of the components of $\overline{R_{ij}}$ at $t = 60$.

DNS and its relative magnitude is less than those of P_k and E_v.

Several components of the planar averaged values of the SGS anisotropy tensor, $\overline{a_{ij}} = \overline{\tau_L(u_i, u_j)} - \frac{2}{3}\overline{k}\delta_{ij}$ are presented in Figs. 15 and 16. Both the Smagorinsky and the dynamic model under-predict the components of this stress. The VFDF predictions are more satisfactory. In this regard, the VFDF is expected to be more effective than the other closures for LES of reacting flows since the extent of SGS mixing is influenced by SGS convection.[69,70] "Optimum" values for C_ε and C_0 cannot be suggested to predict all of the components of this tensor at all times, but it is obvious that there is too much SGS energy with $C_\varepsilon = 0.5$.

Several components of the resolved stress tensor $\overline{R_{ij}}$ are shown in Figs. 17 and 18. As expected, the performance of the Smagorinsky model is not very good as it does not predict the spread and the peak value of the resolved Reynolds stresses. None of the other models show a distinct superiority in predicting the DNS results. The no-model and the dynamic Smagorinsky model predict large peak values at the middle of the layer. The VFDF predicts both the spread and the peak values reasonably well. The results for small C_ε values are not shown since the amount of energy in the re-
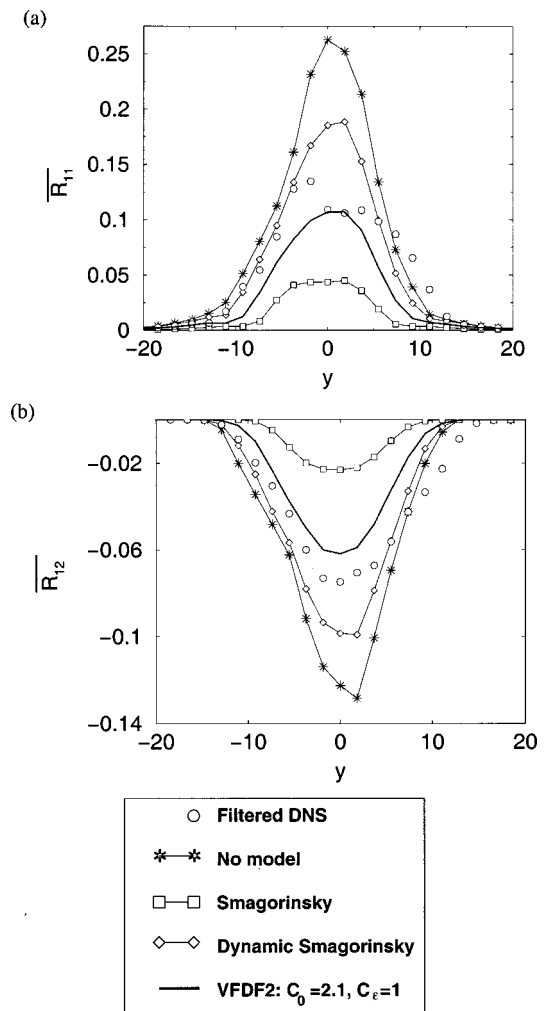
solved scale decreases too much in favor of the increase of the SGS stress (as shown in Figs. 15 and 16). The cross-stream variations of the total Reynolds stress $\overline{r_{12}}$ are presented in Fig. 19. The peak values by the no-model simulations are again the highest. The dynamic model and VFDF perform similarly and capture the DNS trends equally well.

E. Comparison with previous investigations

All of the results obtained here by DNS, and LES via the Smagorinsky and the dynamic Smagorinsky models agree very well with those of Vreman et al.[20] The slight differences are due to the nonidentical flow initializations, and the different computational methodologies employed in the two simulations. To compare with results of other investigations, simulations are conducted of another temporally developing mixing layer with $Re = 500$ in a larger computational domain, $L_r = 120$. An initial forcing of the form $\mathcal{A}e^{-(y/2)^2}$ is used, where $\mathcal{A}$ is a uniformly distributed random number with an amplitude of 0.05. Rogers and Moser[60] perform DNS of a high Re number flow on $512 \times 210 \times 192$ spectral points. The results of these simulations are in excellent agreements with laboratory data of Bell and Mehta.[71] Here, LES is con

(a)

(b)

○—○ **Filtered DNS**

＊—＊ **No model**

□—□ **Smagorinsky**

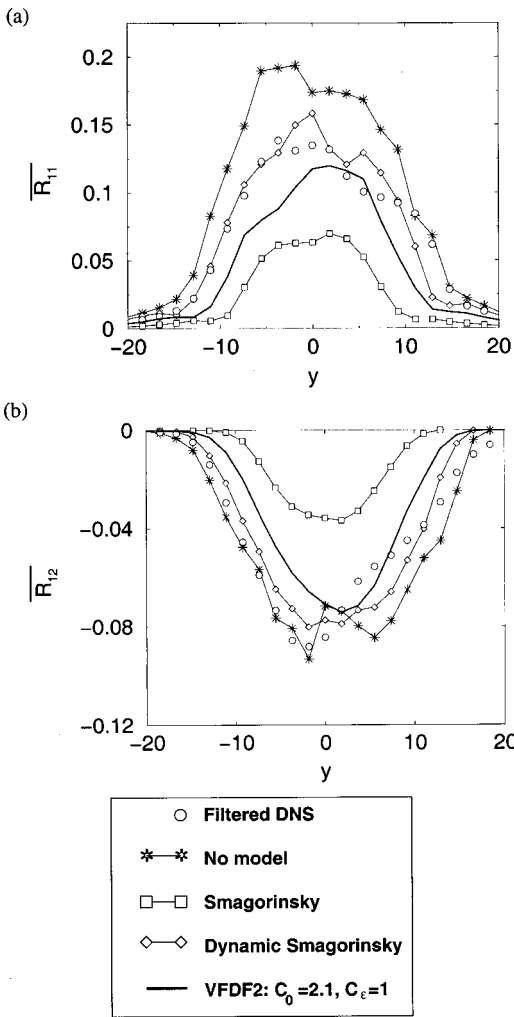◇—◇ **Dynamic Smagorinsky**

—— **VFDF2: C₀ =2.1, Cₑ=1**

FIG. 18. Cross-stream variations of some of the components of $\overline{R_{ij}}$ at t =80.

ducted of this flow via the dynamic Smagorinsky model.

The profiles of the mean streamwise velocity and several components of the resolved stresses at $t=250$ are presented in Figs. 20 and 21, respectively. In these figures, $\xi = y/\delta_m(t)$ and the symbols denote the experimental data[71] at several streamwise locations. The good agreement with these data also indicates good agreement with DNS results of Rogers and Moser.[72]

F. Computational requirements

The total computational times associated with simulations of the 3D temporal mixing layer are shown in Table II. Expectedly, the overhead associated with the VFDF simulation is extensive as compared to the other models; nevertheless this requirement is significantly less that of DNS. This overhead was tolerated in present simulations, but can be reduced with utilization of an optimum parallel simulation procedure. This has been discussed for use in PDF[73] and is recommended for future VFDF simulations.

VII. SUMMARY AND CONCLUDING REMARKS

The filtered density function (FDF) methodology[1] has proven very effective for large eddy simulation (LES) of

(a)

(b)

○ **Filtered DNS**

● **Unfiltered DNS**

＊—＊ **No model**

□—□ **Smagorinsky**
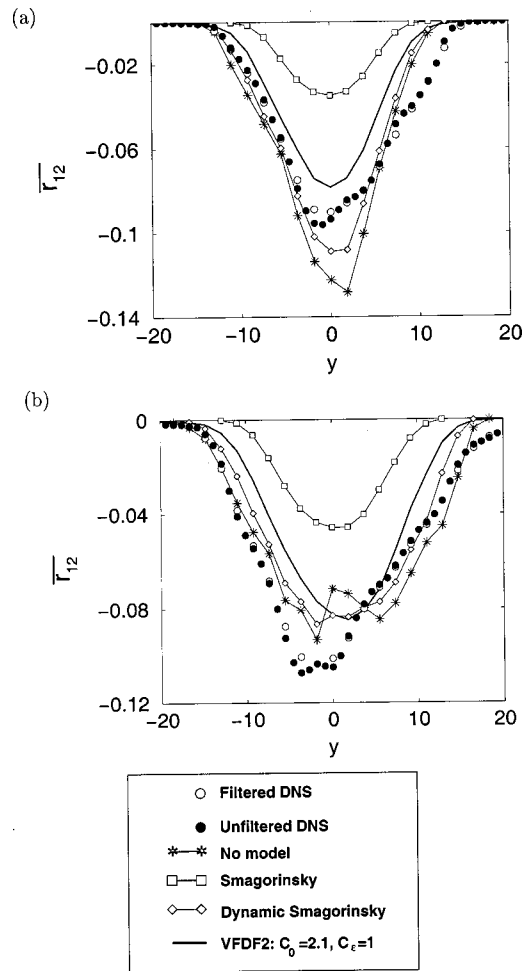
◇—◇ **Dynamic Smagorinsky**

—— **VFDF2: C₀ =2.1, Cₑ=1**

FIG. 19. Cross-stream variations of $\overline{r_{12}}$, (a) $t=60$, (b) $t=80$.

turbulent reacting flows.[3,6–11] In all previous contributions, the LES/FDF of only the scalar quantities are considered. The objective of the present work is to develop the FDF methodology for LES of the velocity field. For this purpose, a methodology termed the velocity filtered density function
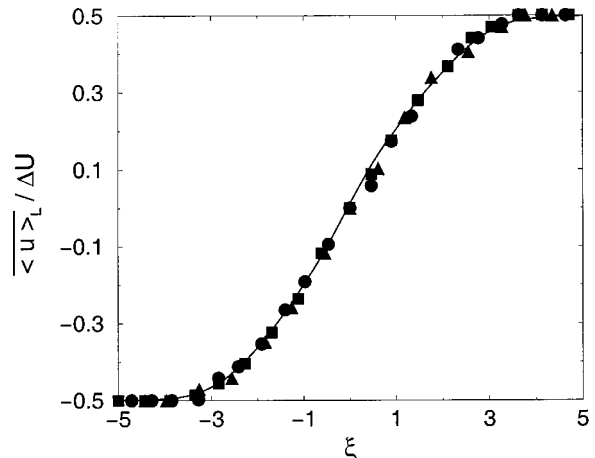

FIG. 20. Cross-stream variation of the Reynolds averaged values of the streamwise velocity at $t=250$. Solid line denotes model predictions via the dynamic Smagorinsky model. Symbols denote experimental data of Bell and Mehta (Ref. 71).
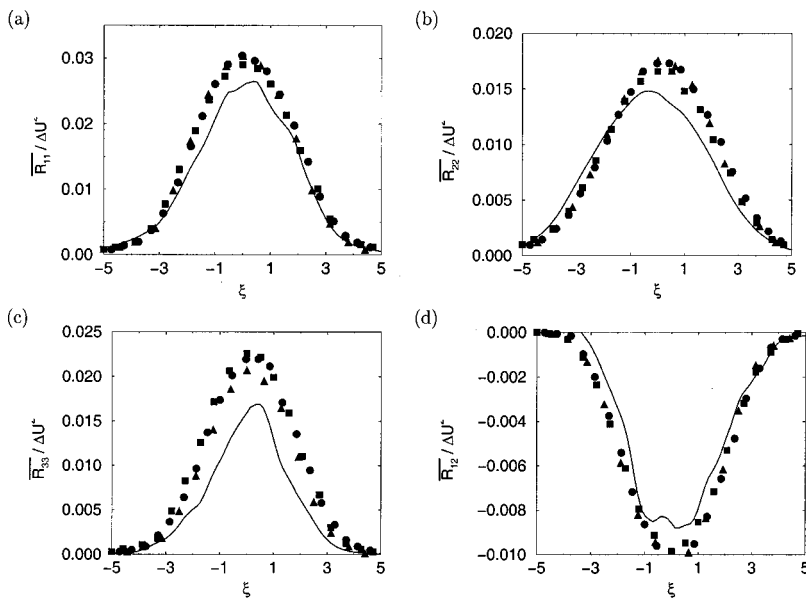
FIG. 21. Cross-stream variations of the Reynolds averaged values of the streamwise velocity at $t=250$. Solid lines denote model predictions via the dynamic Smagorinsky model. Symbols denote experimental data of Bell and Mehta (Ref. 71).

(VFDF) is developed. The VFDF is basically the probability function (PDF) of the subgrid scale (SGS) velocity vector. The exact transport equation governing the evolution of the VFDF is derived. It is shown that the effects of SGS convection in this equation appears in a closed form. The unclosed terms in this transport equation are modeled via two formulations: VFDF1 and VFDF2. The primary difference between the two models is the inclusion of the molecular diffusion in the spatial transport of the VFDF in the first formulation. The closure strategy in the formulation similar to that in PDF methods in Reynolds averaged simulation (RAS) procedures.[32] In this way, the VFDF formulation is at least equivalent to a second-order moment SGS closure.

The modeled VFDF transport equations are solved numerically via a Lagrangian Monte Carlo scheme in which the solutions of the equivalent stochastic differential equations (SDEs) are obtained. Two Monte Carlo procedures are considered. The schemes preserve the Itô–Gikhman nature of the SDEs and provide a reliable solution for the VFDF. The consistency of the VFDF formulation and the convergence of its Monte Carlo solutions are assessed. This is done via comparisons between the results obtained by the Monte Carlo procedure and the finite difference solution of the transport equations of the first two filtered moments of VFDF (LES-FD). With inclusion of the third moments from the VFDF into the LES-FD, the consistency and convergence of the

Monte Carlo solution is demonstrated by good agreements of the first two SGS moments with those obtained by LES-FD.

The VFDF predictions are compared with those with LES results with no SGS model, with the Smagorinsky[16] SGS closure, and with the dynamic Smagorinsky[17–19] model. All of these results are also compared with direct numerical simulation (DNS) results of a three-dimensional, temporally developing mixing layer in a context similar to that conducted by Vreman et al.[20] This comparison provides a means of examining some of the trends and overall characteristics as predicted by LES. It is shown that the VFDF performs well in predicting some of the phenomena pertaining to the SGS transport. The magnitude of the SGS Reynolds stresses as predicted by VFDF is larger than those predicted by the other SGS models and much closer to the filtered DNS results. The temporal evolution of the production rate of the SGS kinetic energy is predicted well by VFDF as compared with those via the other closures. The VFDF is also capable of accounting the SGS backscatter without any numerical instability problems, although the level predicted is substantially less than that observed in DNS.

The results of *a priori* assessment against DNS data indicates that the values of the model coefficients as employed in VFDF (C_0 and C_ε) are of the range suggested in the equivalent models previously used in RAS. The results of *a posteriori* assessments via comparison with DNS data does not give any compelling reasons to use values other than those suggested in RAS, $C_0=2.1$, $C_\varepsilon=1$. However, small values of C_ε are not acceptable as they would yield too much of SGS energy relative to that within the resolved scales.

Most of the overall flow features, including the mean velocity field and the resolved and total Reynolds stresses as predicted by VFDF are similar to those obtained via the dynamic Smagorinsky model. This is interesting in view of the fact that the model coefficients in VFDF are kept fixed. It may be possible to improve the predictive capabilities of the VFDF by two ways: (1) Development of a dynamic proce-

TABLE II. Computer requirements for the 3D temporal mixing layer. One unit corresponds to 1657.2 seconds of CPU time on the SGI origin 2000.

	Resolution	N_E	Normalized CPU time
DNS	$193\times193\times193$	⋯	178
VFDF1	$33\times33\times33$	40	33.6
VFDF2	$33\times33\times33$	40	30
Dynamic Smagorinsky	$33\times33\times33$	⋯	2.19
Smagorinsky	$33\times33\times33$	⋯	1.05
No model	$33\times33\times33$	⋯	1

dure to determine the model coefficients, and/or (2) implementation of higher order closures for the generalized Langevin model parameter G_{ij} (see Ref. 34).

Work is in progress towards developments of a joint velocity-scalar FDF for LES of reacting flows. Compared to standard LES, this approach has the advantage of treating reaction in a closed form; and, compared to scalar FDF[6,8] has the advantage of treating convective transport (of momentum and species) in closed form. These modeling advantages have an associated computational penalty. For the cases considered here, VFDF is more expensive computationally than the dynamic Smagorinsky model by a factor of 15. It is expected that VFDF will not be more expensive than scalar FDF, at least for reacting flows with many species.

[1] S. B. Pope, "Computations of turbulent combustion: Progress and challenges," Proc. Combust. Inst. **23**, 591 (1990).

[2] C. K. Madnia and P. Givi, "Direct numerical simulation and large eddy simulation of reacting homogeneous turbulence," in *Large Eddy Simulations of Complex Engineering and Geophysical Flows*, edited by B. Galperin and S. A. Orszag (Cambridge University Press, Cambridge, UK, 1993), pp. 315–346.

[3] F. Gao and E. E. O'Brien, "A large-eddy simulation scheme for turbulent reacting flows," Phys. Fluids A **5**, 1282 (1993).

[4] S. H. Frankel, V. Adumitroaie, C. K. Madnia, and P. Givi, "Large eddy simulations of turbulent reacting flows by assumed PDF methods," Engineering Applications of Large Eddy Simulations **162**, 81 (1993).

[5] A. W. Cook and J. J. Riley, "A subgrid model for equilibrium chemistry in turbulent flows," Phys. Fluids **6**, 2868 (1994).

[6] P. J. Colucci, F. A. Jaberi, P. Givi, and S. B. Pope, "Filtered density function for large eddy simulation of turbulent reacting flows," Phys. Fluids **10**, 499 (1998).

[7] J. Réveillon and L. Vervisch, "Subgrid scale turbulent micromixing: Dynamic approach," AIAA J. **36**, 336 (1998).

[8] F. A. Jaberi, P. J. Colucci, S. James, P. Givi, and S. B. Pope, "Filtered mass density function for large eddy simulation of turbulent reacting flows," J. Fluid Mech. **401**, 85 (1999).

[9] S. C. Garrick, F. A. Jaberi, and P. Givi, "Large eddy simulation of scalar transport in a turbulent jet flow," in *Recent Advances in DNS and LES, Fluid Mechanics and its Applications*, edited by D. Knight and L. Sakell (Kluwer Academic, Dordrecht, 1999), Vol. 54, pp. 155–166.

[10] S. James and F. A. Jaberi, "Large scale simulations of two-dimensional nonpremixed methane jet flames," Combust. Flame **123**, 465 (2000).

[11] S. B. Pope, *Turbulent Flows* (Cambridge University Press, Cambridge, UK, 2000).

[12] X. Y. Zhou and J. C. F. Pereira, "Large eddy simulation (2D) of a reacting plan mixing layer using filtered density function," Flow, Turbul. Combust. **64**, 279 (2000).

[13] K. H. Luo, "DNS and LES of turbulence-combustion interactions," in Ref. 22, Chap. 14, pp. 263–293.

[14] T. Poinsot and D. Veynante, *Theoretical and Numerical Combustion* (R. T. Edwards, Philadelphia, 2001).

[15] C. Tong, "Measurements of conserved scalar filtered density function in a turbulent jet," Phys. Fluids **13**, 2923 (2001).

[16] J. Smagorinsky, "General circulation experiments with the primitive equations. I. The basic experiment," Mon. Weather Rev. **91**(3), 99 (1963).

[17] M. Germano, U. Piomelli, P. Moin, and W. H. Cabot, "A dynamic subgrid-scale eddy viscosity model," Phys. Fluids A **3**, 1760 (1991).

[18] M. Germano, "Turbulence: The filtering approach," J. Fluid Mech. **238**, 325 (1992).

[19] D. K. Lilly, "A proposed modification of the Germano sub-grid closure method," Phys. Fluids A **4**, 633 (1992).

[20] B. Vreman, B. Geurts, and H. Kuerten, "Large-eddy simulation of the turbulent mixing layer," J. Fluid Mech. **339**, 357 (1997).

[21] A. A. Aldama, *Filtering Techniques for Turbulent Flow Simulations, Lecture Notes in Engineering, Vol. 49* (Springer-Verlag, New York, 1990).

[22] *Modern Simulation Strategies for Turbulent Flow*, edited by B. J. Geurts (R. T. Edwards, Philadelphia, 2001).

[23] P. Sagaut, *Large Eddy Simulation for Incompressible Flows* (Springer, New York, 2001).

[24] B. Vreman, B. Geurts, and H. Kuerten, "Realizability conditions for the turbulent stress tensor in large-eddy simulation," J. Fluid Mech. **278**, 351 (1994).

[25] E. E. O'Brien, "The probability density function (PDF) approach to reacting turbulent flows," in *Turbulent Reacting Flows*, edited by P. A. Libby and F. A. Williams (Springer-Verlag, Heidelberg, 1980), Chap. 5, pp. 185–218.

[26] S. B. Pope, "PDF methods for turbulent reacting flows," Prog. Energy Combust. Sci. **11**, 119 (1985).

[27] D. C. Haworth and S. B. Pope, "A generalized Langevin model for turbulent flows," Phys. Fluids **29**, 387 (1986).

[28] D. C. Haworth and S. B. Pope, "A PDF modeling study of self-similar turbulent free shear flows," Phys. Fluids **30**, 1026 (1987).

[29] T. D. Dreeben and S. B. Pope, "Probability density function and Reynolds-stress modeling of near-wall turbulent flows," Phys. Fluids **9**, 154 (1997).

[30] T. D. Dreeben and S. B. Pope, "Wall-function treatment in PDF methods for turbulent flows," Phys. Fluids **9**, 2692 (1997).

[31] T. D. Dreeben and S. B. Pope, "Probability density function/Monte Carlo simulation of near-wall turbulent flows," J. Fluid Mech. **357**, 141 (1998).

[32] S. B. Pope, "Lagrangian PDF methods for turbulent flows," Annu. Rev. Fluid Mech. **26**, 23 (1994).

[33] J. Rotta, "Statistiche theorie nichththomogener turbulenz," J. Zeitsch fur Physik **129**, 547 (1951) [translation in English available in NASA TM-14560 (1982)].

[34] S. B. Pope, "On the relationship between stochastic Lagrangian models of turbulence and second-moment closures," Phys. Fluids **6**, 973 (1994).

[35] J. W. Deardorff, "The use of subgrid transport equations in a three-dimensional model of atmospheric turbulence," J. Fluids Eng. **95**, 429 (1973).

[36] H. Risken, *The Fokker–Planck Equation, Methods of Solution and Applications* (Springer, New York, 1989).

[37] C. W. Gardiner, *Handbook of Stochastic Methods* (Springer-Verlag, New York, 1990).

[38] S. Karlin and H. M. Taylor, *A Second Course in Stochastic Processes* (Academic, New York, 1981).

[39] S. B. Pope, "Mean field equations in PDF particle methods for turbulent reactive flows," Technical Report FDA 97-06, Sibley School of Mechanical and Aerospace Engineering, Cornell University, Ithaca, NY, 1997.

[40] M. Muradoglu, P. Jenny, S. B. Pope, and D. A. Caughey, "A consistent hybrid-volume/particle method for the PDF equations of turbulent reactive flows," J. Comput. Phys. **154**, 342 (1999).

[41] M. Muradoglu, S. B. Pope, and D. A. Caughey, "The hybrid method for the PDF equations of turbulent reactive flows: Consistency conditions and correction algorithms," J. Comput. Phys. **172**, 841 (2001).

[42] P. E. Kloeden and E. Platen, *Numerical Solution of Stochastic Differential Equations, Applications of Mathematical Stochastic Modelling and Ap-*

plied Probability, Vol. 23 (Springer-Verlag, New York, 1995).

[43]P. Billingsly, *Probability and Measure* (Wiley, New York, 1979).

[44]D. T. Gillespie, *Markov Processes, An Introduction for Physical Scientists* (Academic, New York, 1992).

[45]K. Itô, *Differential Equations, Memoirs of the American Mathematical Society, Vol. 4* (American Mathematical Society, Providence, RI, 1951).

[46]I. I. Gikhman and A. V. Skorokhod, *Stochastic Differential Equations* (Academic, New York, 1972).

[47]M. H. Carpenter, "A high-order compact numerical algorithm for supersonic flows," in *Proceedings of the 12th International Conference on Numerical Methods in Fluid Dynamics, Lecture Notes in Physics*, edited by K. W. Mortron (Springer-Verlag, Berlin, 1990), Vol. 371, pp. 254–258.

[48]R. W. MacCormack, "The effect of viscosity in hypervelocity impact catering," AIAA Paper AIAA-69-354 (1969).

[49]T. J. Poinsot and S. K. Lele, "Boundary conditions for direct simulations of compressible viscous flows," J. Comput. Phys. **101**, 104 (1992).

[50]D. H. Rudy and J. C. Strikwerda, "Boundary conditions for subsonic compressible Navier–Stokes calculations," J. Comput. Phys. **36**, 327 (1980).

[51]J. J. Riley and R. W. Metcalfe, "Direct numerical simulations of a perturbed, turbulent mixing layer," AIAA Paper AIAA-80-0274 (1980).

[52]N. D. Sandham and W. C. Reynolds, "Three-dimensional simulations of large eddies in the compressible mixing layer," J. Fluid Mech. **224**, 133 (1991).

[53]R. D. Moser and M. M. Rogers, "The three-dimensional evolution of a plane mixing layer: Pairing and transition to turbulence," J. Fluid Mech. **247**, 275 (1993).

[54]R. W. Metcalfe, S. A. Orszag, M. E. Brachet, S. Menon, and J. J. Riley, "Secondary instabilities of a temporally growing mixing layer," J. Fluid Mech. **184**, 207 (1987).

[55]S. J. Lin and G. M. Corcos, "The mixing layer: Deterministic models of a turbulent flow. Part 3. The effect of plane strain on the dynamics of streamwise vortices," J. Fluid Mech. **141**, 139 (1984).

[56]R. D. Moser and M. M. Rogers, "The three-dimensional evolution of a plane mixing layer: The Kelvin–Helmholtz rollup," J. Fluid Mech. **243**, 183 (1992).

[57]R. D. Moser and M. M. Rogers, "Spanwise scale selection in plane mixing layers," J. Fluid Mech. **247**, 321 (1993).

[58]J. H. Ferziger, "Higher level simulations of turbulent flows," Stanford University Report TF-16, Department of Mechanical Engineering, Stanford University, Stanford, CA, 1981.

[59]G. Erlebacher, M. Y. Hussaini, C. G. Speziale, and T. A. Zang, "Toward the large eddy simulation of compressible turbulent flows," J. Fluid Mech. **238**, 155 (1992).

[60]R. S. Rogallo and P. Moin, "Numerical simulation of turbulent flow," Annu. Rev. Fluid Mech. **16**, 99 (1984).

[61]J. W. Deardorff, "On the magnitude of the subgrid scale eddy coefficient," J. Comput. Phys. **7**, 120 (1971).

[62]U. Piomelli, "Large-eddy simulation: Achievements and challenges," Prog. Aerosp. Sci. **35**, 335 (1999).

[63]C. Meneveau and J. Katz, "Scale-invariance and turbulence models for large-eddy simulations," Annu. Rev. Fluid Mech. **32**, 1 (2000).

[64]U. Piomelli, W. H. Cabot, P. Moin, and S. Lee, "Subgrid-scale backscatter in turbulent and transitional flows," Phys. Fluids A **3**, 1766 (1991).

[65]P. J. Mason and D. J. Thomson, "Stochastic backscatter in large eddy simulation of boundary layers," J. Fluid Mech. **242**, 51 (1992).

[66]D. Carati, S. Ghosal, and P. Moin, "On the representation of backscatter in dynamic localization models," Phys. Fluids **7**, 606 (1995).

[67]M. Germano, "A statistical formulation of the dynamic model," Phys. Fluids **8**, 565 (1996).

[68]J. W. Deardorff, "A numerical study of three-dimensional turbulent channel flow at large Reynolds number," J. Fluid Mech. **41**, 453 (1970).

[69]R. W. Bilger, "Future progress in turbulent combustion research," Prog. Energy Combust. Sci. **26**, 367 (2000).

[70]N. Peters, *Turbulent Combustion* (Cambridge University Press, Cambridge, UK, 2000).

[71]J. H. Bell and R. D. Metha, "Development of a two-stream mixing layer from tripped and untripped boundary layer," AIAA J. **28**, 2034 (1990).

[72]M. M. Rogers and R. D. Moser, "Direct simulation of a self-similar turbulent mixing layer," Phys. Fluids **6**, 903 (1994).

[73]A. D. Leonard and F. Dai, "Applications of a coupled Monte Carlo PDF/finite volume, CFD method for turbulent combustion," AIAA Paper AIAA-94-2904 (1994).